Title
Measuring and Modeling Self-Assembly in Cardiomyocytes

Author
Drew, Nancy Kimberly

Publication Date
2016

Peer reviewed|Thesis/dissertation

UNIVERSITY OF CALIFORNIA,
IRVINE

Measuring and Modeling Self-Assembly in Cardiomyocytes

DISSERTATION

submitted in partial satisfaction of the requirements
for the degree of

DOCTOR OF PHILOSOPHY

in Biomedical Engineering

by

Nancy Kimberly Drew

Dissertation Committee:
Assistant Professor Anna Grosberg, Chair
Assistant Professor Michelle Digman
Assistant Professor Jun Allard

2016

TABLE OF CONTENTS

LIST OF FIGURES

Page

LIST OF TABLES

ACKNOWLEDGMENTS

I would like to thank my family and friends for supporting me through this journey.

This research was supported by the National Institute of Biomedical Imaging and Bioengineering, National Research Service Award EB009418 from the University of California, Irvine, Center for Complex Biological Systems, and National Science Foundation EAGER award No. 1338609.

Also, I would like to thank Danny Baldo Jr., Zachery Robinson, Tuyetnhi Le, Marlen Tagle Rodriguez, and Priyanka Ganesh for participating in gathering single cell data used in this work.

Lastly, I would like to acknowledge the publishers of PLoS Computional Biology and the Journal of Biomechanical Engineering for allowing me to incorporate my previous work in my dissertation. Chapter 2 was published with the permission of Public Library of Science (PLOS). The text and figures of this chapter is a reprint of the material as it appears in PLoS Computional Biology. I also thank ASME for permission to include sections in Chapter 3 of my dissertation, which was originally published in Journal of Biomechanical Engineering.

CURRICULUM VITAE

Nancy Kimberly Drew

EDUCATION

Doctor of Philosophy in Biomedical Engineering **2016**
University of California, Irvine *Irvine, CA*

Master of Science in Biomedical Engineering **2015**
University of California, Irvine *Irvine, CA*

Bachelor of Science in Mathematics **2010**
Sweet Briar College *Sweet Briar, VA*

RESEARCH EXPERIENCE

Graduate Research Assistant **2011–2016**
University of California, Irvine *Irvine, California*

REFEREED JOURNAL PUBLICATIONS

Metrics for Assessing Cytoskeletal Orientational Correlations and Consistency **2015**
PLoS Computional Biology

Methods of Myofibrillogenesis Modeling **2015**
Cardiomyocytes: Methods and Protocols

Emergent Global Contractile Force in Cardiac Tissues **2016**
Biophysical Journal

Multi-Scale Characterization of Engineered Cardiac Tissue Architecture **accepted 2016**
Journal of Biomechanical Engineering

ABSTRACT OF THE DISSERTATION

Measuring and Modeling Self-Assembly in Cardiomyocytes

By

Nancy Kimberly Drew

Doctor of Philosophy in Biomedical Engineering

University of California, Irvine, 2016

Assistant Professor Anna Grosberg, Chair

Myofibrillogenesis is the formation of myofibrils, the building blocks of muscle filaments. How neonatal rat ventricular myocytes and human induced-pluripotent stem cell (iPS) derived cardiomyocytes assemble will have a great impact on tissue engineering strategies for building myocardium *in vitro*. Normally, cardiomyocytes cultured on extracellular matrix islands form myofibrils that extend across the longest diagonal of the cells, but this is not necessarily the case for iPS-derived cardiomyocytes. In order to investigate why this is not always the case, it is advantageous to examine the self-assembly mechanism *in vitro* by quantifying the consistency of changes in cardiomyocyte architecture in response to a variety of input conditions. We developed the Co-orientational order parameter (COOP) to quantify the correlation between orientations of biological constructs and the consistency of cytoskeleton architecture. Using this newly invented parameter, we were able to investigate consistency across multiple length scales. To further explore this topic, microcontact printing was used to create cells of specific shapes (i.e. triangles, rectangles, squares, ovals, and circles) which were quantified for consistency through image analysis using the COOP. The images of these cells were used to determine at which length scales cardiomyocyte self-assembly was consistent and to fit and validate a computational myofibrillogenesis model developed previously in our lab. In the future, this model could be used to help uncover mechanisms of self-assembly of neonatal rat ventricular myocytes and human iPS-derived cardiomyocytes.

Chapter 1

Introduction

In the United States, one of the leading causes of death over the last decade is heart disease [13]. The American Heart Association has predicted that approximately 44% of the United States population will have a form of cardiovascular disease by the year 2030. High blood pressure, high cholesterol, and smoking are some of the risk factors for heart disease. According to the CDC about 50% of Americans have one of these three risk factors [13]. Each year, billions of dollars are spent on treating heart disease [53]. Over the years, scientists, and doctors have made sufficient strides to increase the amount of information known about heart disease and healthy hearts. In additon, many treatment methods have been designed as well. One of the methods with the most promise for treating and developing drugs for heart disease currently being used by some researchers involves using induced-pluripotent stem cell (iPS) derived heart cells [26, 62]. The iPS derived heart cells are an attractive option since embryos are not destroyed during their production, and they can also be specific to the individual patient [67]. In a perfect world, iPS derived heart cells could be used to fully rebuild the myocardium. While iPS derived heart cells have been helpful in cardiac research, they are still inadequate as a true substitute for heart cells (cardiomyocytes) because this cell type does not have all of the structural and functional

properties of healthy cardiomyocytes [42, 61].

1.1 Background

1.1.1 Organization and Structures in the Heart

Healthy hearts have structures that are intricately organized at multiple length scales. At the tissue scale, multiple cardiac sheets form muscular heart walls that work symbiotically to contract and relax the heart [14]. The same organization scheme extends to the cellular scale, with myofibrils arranged into bundles, and further at the intracellular scale, where multiple repeats of sarcomeres form these myofibrils [2]. Sarcomeres, which are composed of z-lines and actin-fibrils are the contractile units of the cell, and contractility is an essential property of heart function, as observed at the tissue scale [2].

Besides containing myofibrils, cardiomyocytes architecture also consists of an arrangement of focal adhesions [9]. Focal adhesions help connect cardiomycoytes to the extracellular matrix (ECM) and provide cardiomyocytes with details about the conditions of the ECM. The complexes that make focal adhesions consist of engaged (bound) integrins. Through integrins, focal adhesions are connected to actin filaments, which are embodied in myofibrils [2, 39]. In summary, bundles of myofibrils span the longest diagonal of cultured isolated myocytes, with focal adhesions at the periphery of the cell which are concentrated at the corners of cultured isolated cardiomyocytes [9].

1.1.2 Conditions Influencing Organization

Mechanotransduction, migration, and boundary conditions have all been shown to influence self-assembly of intracellular structures [61, 9]. The cells' organization of the intracellular

structure depends on the cellular response to geometrical boundaries, cell shape, migration cues, stretching, and other chemical or physical cues [61]. For example, when engineered cardiac tissues are stretched actin and sarcomere orientation is affected and cells will align with the direction of the stretch [50]. Cell shape is a static cue that is controlled by the ECM boundary conditions. Previously, it was observed experimentally that a cells internal structure is a function of geometrical cues. Triangular and square shaped cells have myofibrils that span the longest diagonals of the cells [9, 32]. Whereas, when the aspect ratio increases and squares become long rectangular cells, myofibrils are longitudinal to the cell [9]. Circular cells are an example of a rotationally symmetric shape, and the organization of myofibrils is random [9] but can be polarized.

1.1.3 Organization in Heart Disease

During heart disease, organization is disrupted at some of these scales and pumping is affected [37, 76, 3]. For example, at the tissue scale cardiac tissue can be disorganized with bundles of myofibrils scattered in numerous orientations. Additionally, organization can be effected at the cellular scale, myocytes can change shape and there is often a change in length to width ratio or aspect ratio [29]. It has been shown that the cellular aspect ratio is a function of contractility in single cells, and traction force microscopy data has demonstrated that the maximum force is produced by cardiomyocytes with an aspect ratio of 6-7 [47]. However, it is not known if cells of certain shapes are more consistent in their self-assembly [28]. Gerdes et al. reported that cells with elongated shapes are endemic for various types of heart disease [29]. Since cell shape influences organization, it is necessary to quantify intracellular architecture self-assembly of cardiomyocytes for different shaped cells at multiple scales in order to provide information that can be used to predict the mechanisms involved in heart disease.

1.2 Overview of Present Models

One technique used to predict and explain cell behavior is through computational model. Boundary conditions are an attractive variable for early fibrillogenesis (formation of fibrils) modeling because they can be manipulated *in vitro* e.g. cell shape [9, 32, 56], and patterned surfaces [45, 23, 24]. Previously, numerous types of cell myofibrillogenesis computational models were created. One example is a phenomenological model based on focal adhesion distribution in the cell created by Novak et al. [55]. This model forecasts a high concentration of focal adhesion at the edges of the cell validated by experimental data from NIH3T3 fibroblast [55]. Novak et al.'s model did not include a myofibril length-developed tension relationship, the maturation of fibrils, or mechanical properties of the substrate [55]. Another type of model is a finite element model of the distribution of myofibrils designed by Deshpande et al. [18, 19]. This model is based on the interaction among integrins, the substrate, and stress fibers [18, 19]. Additionally, the model can predict the distribution of myofibrils in a variety of cell shapes. However, fibroblast and epithelial cells were used to validate this computationally complex model, which is problematic as cardiomyocytes are inherently different in both structure and function when compared to fibroblast and epithelial cell lines. Paszek et al., created a chemo-mechanical model based on the interaction between ligands and integrins [57]. This model can predict the stresses and strains of focal adhesions, however it was not validated with a specific cell type. Paszek et al.'s model does not include myofibrils and stress fibers. Our lab previously created a phenomenological model of myofibrillogenesis [32]. This model is based on the interaction between myofibrils and focal adhesions and uses the concepts in Novak et al.'s model [32]. Unlike the models presented by Deshpande et al. and Paszek et al., it is specific to cardiomyocytes and was validated using *in vitro* data obtained from neonatal rat ventricular myocytes. The model's purpose is to explore how symmetry breaking and boundary conditions affect self-assembly.

Despite the creation of multiple myofibrillogenesis models, the mechanisms behind how structures inside cardiomyocytes self-assemble are not fully understood. Understanding the mechanisms behind self-assembly could allow for better control when creating engineered cardiac tissues or cardiac patches from stem cell derived heart cells. These tissues and patches could be used to fix the heart and to test drugs for heart disease therapies [62, 26]. Currently, recapitulating the multi-scale organization seen in healthy hearts is one challenge that still remains when utilizing stem cell derived cardiomyocytes [62, 26]. In order to explore self-assembly in heart cells, tools and metrics are needed to quantify organization at a variety of length scales.

1.3 Metrics to Quantify Organization

Previously the process of quantifying orientation of structures in images was performed manually [40] or by using a variety of computational algorithms [10, 43, 23, 77]. Later, after identifying the orientation of the structures through image analysis, these studies selected a metric to summarize the overall organization. For example, a study by Davidson et al. on human osteoprogenitor (HOP) cells on grooved surfaces used an orientation metric that provides the standard deviation of a truncated Gaussian distribution [17]. Studies done by Karlon et al. to analyze orientation in endothelial cells and Dunn et al. to analyze fibroblast alignment on grooved surfaces used metrics based on the von Mises circular distribution [43, 23]. However, the von Mises circular distribution is a wrapped normal (Gaussian) distribution and often subcellular structures distributions are non-gaussian. Therefore, it is not ideal to use these distributions to analyze organization of subceullular distributions.

Others used an alternative metric called the orientational order parameter (OOP) [24, 75, 66, 72, 31, 45]. The OOP was originally developed for the field of liquid crystals [34] and applied to other areas for quantifying the organization of subcellular structures in cardiac

tissues and cardiomyocytes [31, 45], fibroblast cells [66], valve endothelial cells [6], bacteria [75], and vascular smooth muscle cells [72]. Even though this metric has been widely used, it is not capable of determining correlation of two subcellular structures or the consistency of one subcellular structure.

Prior studies have used a variety of metrics to quantify correlation in images. For instance, to compare two images with a change in scale or possible rotation, Feng et al. used normalized cross-correlation [25]. Yet, this method is insensitive to a rotation of the whole images. Another study done by Noorafshan et al. used second-order stereology to analyze the correlation between the spatial arrangement of microvessels and cardiomyocytes [54]. Some studies have used colocalization to analyze the spatial overlap between two biological structures [71, 74]. Nonetheless, second-order stereology or colocalization is capable of analyzing the relative orientations of biological subcellular structures. Lastly, another metric created to analyze correlation is the circular correlation coefficient, which can only be used on data with uniform distributions [7]. All of the above metrics have been used previously, but we need a tool that does not depend on certain distributions and that is capable of analyzing correlation of two subcellular structures as well as analyzing consistency of one subcellular structure.

1.4 Quantify Correlation and Consistency of Subcellular Structures Organization in Cardiomyocytes

In this work, we developed a new metric, the co-orientational order parameter (COOP), to analyze self-assembly of heart cells *in vitro* and *in silico*. Here we present, in Chapter 2, the derivation and theorems to illustrate the properties and boundaries of the COOP.

Additionally, we show an application of the COOP to quantify the correlation of actin fibrils and sarcomeric z-lines in disorganized engineered cardiac tissue. Then, to explore self-assembly we use the COOP in Chapters 3 and 4 to quantify the consistency of subcellular structure organization in cardiomyocytes *in vitro* and *in silico*.

Chapter 2

Metrics for Assessing Cytoskeletal Orientational Correlations and Consistency

[1]

2.1 Introduction

The architecture and organization of the cytoskeleton components in cells, the cells in tissues, and cellular ensembles in organs affect function at each of these physiological scales [65, 32, 12, 58]. The study of architecture is therefore key to understanding how the cellular microenvironment potentiates function, and may provide new insights in the study of physiological mechanisms. Furthermore, for proper function, different components of the cytoskeleton, cell, or tissue need to co-localize and orient properly with respect to each

[1] Drew et al., 2015 PLoS Comput Biol

other [22, 10]. Quantifying the degree of orientation of cells and subcellular components, both relative to themselves and to other components, is thus crucial for evaluating the quality of engineered tissues [62].

The problem of describing the organization of biological structures is twofold: first, the orientation of the constructs needs to be quantified from the available images, and second, a metric needs to be applied to summarize the overall organization. The quantification of orientation from biological images is in principle straightforward and can be either done manually [40] or with a variety of computational algorithms [10, 43, 23, 77]. As far as the second problem is concerned, summarizing the overall organization after image analysis involves selecting a metric, which is more controversial. As a result, a wide variety of metrics are utilized in the bio-imaging field. For example, some assume that the parameter can be described as the standard deviation of a truncated Gaussian, or normal, distribution [17]. Others use the von Mises circular distribution [43, 23], which is a wrapped normal distribution. However, cellular and cytoskeleton distributions are often non-Gaussian, and their being non-Gaussian may be of crucial importance [24].

An alternative metric, the Orientational Order Parameter (OOP), has been developed in the field of liquid crystals. The OOP is a mathematical construct developed to quantify the degree of order in anisotropic medias [34]. Mathematically, the OOP is equivalent to resultant vector length from the circular distribution with a period of π [8]. In biology, the OOP has been successfully employed to characterize organization of bacteria [75], fibroblasts [66], vascular smooth muscle [72], actin fibrils alignment in valve endothelial cells [6], and Z-lines in cardiac muscle [31]. However, there is a lack of a robust correlation metric that has been characterized for use with biological images. The suite of correlation parameters provided by circular statistics are either too limited to be used with cytoskeleton organization or so complex the results are hard to connect back to biological phenotypes [7]. Other correlation metrics are also not ideal for correlating orientations of the cytoskeleton components, and to

date no metric has been developed or specifically characterized for this purpose [54, 25, 35].

In this work, we develop a new parameter with similar mathematical framework as OOP that will characterize both consistency of orientation of a single component and correlation of orientation of two components. As an example, we apply this Co-Orientational Order Parameter (COOP) to compare orientation of Z-lines and actin filaments in a neonatal rat ventricular myocyte (NRVM) monolayer. Lastly, we show how the COOP can be used to measure the consistency of building a cardiomyocyte on a triangular island of extracellular matrix (ECM).

2.2 Materials and Methods

2.2.1 Ethics statement

All animals were treated according to the Institutional Animal Care and Use Committee of UCI guidelines (Animal Experimentation Protocol permit number 2013-3093-0). This protocol met the guidelines for the use of vertebrate animals in research and teaching of the Faculty of Arts and Sciences of UCI. It also followed recommendations of the NIH Guide for the Care and Use of Laboratory Animals and was in accordance with existing federal (9 CFR Parts 1, 2 & 3), state, and city laws and regulations governing the use of animals in research and teaching.

2.2.2 Implementing COOP calculation

To facilitate the calculation of the COOP we created a custom MATLAB code. The code was designed to have an input of angles for P and Q organized such that the information of which pseudo-vectors are paired was not lost. The code outputs were OOP_P, OOP_Q, COOP,

$COOP_u$, $COOP_c$, $\hat{n}$, and θ.

2.2.3 Synthetic data

Synthetic data of isotropic constructs for limiting conditions (Fig. 2.2) was generated using a random number generator (rand) that provides a uniform distribution of at least 10^6 random values in MATLAB. Each construct used in testing $COOP_u$ and $COOP_c$ (Fig. 2.3) contained 10^8 random numbers (MATLAB function normrnd) that were normally distributed with the specified mean and standard deviation.

2.2.4 Experimental data

Microcontact printing and ECM patterns

To make the substrates 25 mm glass coverslips were coated with PDMS (Ellsworth Adhesives, Germantown, WI) and cured for 12 hours in a 60℃ oven. To create triangular myocytes we utilized a microcontact printing procedure similar to that described by Tan et al [68]. A mask with the desired pattern was designed using Adobe Illustrator (Adobe Systems Incorporated, San Jose, CA) and made by Front Range Photomask (Palmer Lake, CO). The mask was used to make a silicone wafer (Integrated Nanosystems Research Facility, Irvine, CA). A polydimethylsiloxane (PDMS) stamp, cast from a silicon master, was used to contact transfer the extracellular matrix (ECM) protein fibronectin (FN) (Fisher Scientific Company, Hanover Park, IL) onto a UV-sterilized (UVO, Jelight Company, Inc. Irvine, CA) PDMS-coated coverslip. Fabricated substrates underwent one 10 minute pluronics (250g of Pluronics F-127, Sigma-Aldrich, Inc., Saint Louis, MO) wash and three rinses of phosphate buffer-saline (PBS) (Life Technologies, Carlsbad, CA). To make isotropic substrates, UV-sterilized PDMS-coated coverslip were coated with FN for 10 minutes and underwent three

PBS washes. The substrates were stored at 4℃prior to NRVM seeding.

Cardiomyocyte culture

Cell cultures of NRVMs were prepared from two-day old Sprague-Dawley rats (Charles River Laboratories, Wilmington, MA). A mid-sternal incision was made in order to expose the heart of the neonatal rat for dissection. Ventricular tissue was removed and rinsed in a Hanks balanced salt solution buffer (Life Technologies, Carlsbad, CA) and placed in 1 mg/mL trypsin solution (Sigma-Aldrich, Inc., Saint Louis, MO) to be shaken overnight (12 hour incubation) at 4℃. The next day, isolated tissue was dissociated into individual cells by treatment with four separate washes of 1 mg/mL collagenase type II (Worthington Biochemical, Lakewood, NJ) for two minutes at 37℃. Isolated cardiomyocytes were resuspended in M199 culture medium (Invitrogen, Carlsbad, CA) supplemented with 10% heat-inactivated Fetal Bovine Serum, 10 mM HEPES, 20 mM glucose, 2 mM L-glutamine, 1.5 µM vitamin B-12 and 50 U/ml penicillin. The cell solution was filtered with a 40 µm filter (Thermo Fisher Scientific, Waltham, MA), and the remaining cells were pre-plated multiple times to eliminate fibroblast contamination. Immediately after purification, myocytes were plated on substrates (prepared as detailed above) at a density of 10^6 or 10^5 cells per well in a standard six-well plate for confluent or sparse cultures, respectively. These were incubated at 37℃ with a 5% CO_2 atmosphere. Seeded cultures underwent a wash with PBS 24 hours after plating to remove unattached and dead myocytes. They were then cultured in 10% serum media for another 24 hours at which point the media was changed to 2% serum media. After a total of 72 hours in culture, the samples were fixed and immunostained.

Fixing, immunostaining and imaging

After 3-4 days in culture, confluent monolayers of cardiomyocytes were fixed with 4% paraformaldehyde (PFA) (VWR, Radnor, PA) with 0.01% Triton X-100 (Sigma-Aldrich, Inc., Saint Louis, MO) for 10 min, and rinsed three times with PBS in 5-min intervals. Cardiomyocytes were stained with nuclei acid-sensitive dye 4',6'-diaminodino-2-phenylinodole (DAPI) (Life Technologies, Carlsbad, CA) for chromatin, FITC-phalloidin (Alexa Fluor 488 Phalloidin, Life Technologies, Carlsbad, CA) for actin, monoclonal mouse sarcomeric anti-α-actinin (Sigma-Aldrich, St. Louis, MO), and polyclonal rabbit anti-human fibronectin (Sigma-Aldrich, St. Louis, MO) and incubated for a total of 1-2 hours at room temperature. Secondary staining was applied using tetramethylrhodamine-conjugated goat anti-mouse IgG antibodies (Alexa Fluor 633 Goat anti-mouse, Life Technologies, Carlsbad, CA) and goat anti-rabbit IgG antibodies (Alexa Fluor 750 goat anti-rabbit, Life Technologies, Carlsbad, CA) for a 1-2 hour incubation. After each incubation period, coverslips were rinsed three times with PBS for 5-10 min. Each coverslip was then mounted onto a microscope slide preserved with prolong gold antifade reagent (Life Technologies, Carlsbad, CA). The images were collected using an IX-83 inverted motorized microscope (Olympus America, Center Valley, PA) with an UPLFLN 40x oil immersion objective (Olympus America, Center Valley, PA) and a digital CCD camera ORCA-R2 C10600-10B (Hamamatsu Photonics, Shizuoka Prefecture, Japan). For isotropic monolayers, at least ten fields of view were collected for every sample.

'Noiseless" image generation

A macro was created in ImageJ that allows the user to select regions without imperfections in an image. The regions that were not selected became masked, resulting in a series of images with only regions of interest displayed in the new masked images for every channel

imaged (for example: DAPI, m-cherry, GFP)(Fig. 2.4). The masked images could then be analyzed using the same codes used for raw images.

Calculating construct angles

To determine construct angles, we adapted a previous MATLAB code that detects ridges of a fingerprint [31, 46, 38]. This code was used to detect Z-lines and actin fibers in the images. In the code, a binary mask applied to the image determined the constructs and a filter was applied to clean up the constructs that were identified in the images. The code took pixel information from the images and for every non-empty pixel in the image, a pseudo-vector was calculated and used to determine the OOP for Z-lines and actin fibrils, as well as a new set of pseudo-vectors for each square in the grid (Fig. 2.4B,D) These new pseudo-vectors were then utilized to calculate the COOP between two constructs (i.e. Z-lines and actin fibrils) or two cells (Fig. 2.4).

Statistics

To calculate the average angle between the constructs ($\langle\theta_0\rangle$) and the standard deviation of those angles (σ_{θ_0}) across multiple conver-slips, it is essential to keep in mind that the angle period is π. The simplest way, but not the only way, to generate $\langle\theta_0\rangle$ and σ_{θ_0} is to calculate the director of the director pseudo-vectors $\hat{\mathrm{n}}_{\mathrm{ALL}}$ of each cover-slip. Meaning that in Eq. (2.2) $\overrightarrow{k_i}=\hat{\mathrm{n}}_{\mathrm{i}}$ where i is the cover-slip, and the $\hat{\mathrm{n}}_{\mathrm{ALL}}$ is the the eigenvector of the tensor from Eq. (2.2) that corresponds to the eigenvalue from Eq. (2.3). The angle for each cover-slip is then determined as follows

$$\theta_{0,i} = \begin{cases} arccos(\hat{n}_i) & \text{for } \frac{\pi}{4} < arccos(\hat{n}_{ALL}) < \frac{3\pi}{4} \\ arcsin(\hat{n}_i) & \text{for } arccos(\hat{n}_{ALL}) > \frac{3\pi}{4} \text{ or } arccos(\hat{n}_{ALL}) < \frac{\pi}{4}. \end{cases} \tag{2.1}$$

The $\langle\theta_0\rangle$ and σ_{θ_0} are the average and standard deviation of $\theta_{0,i}$ for all cover-silps. Obviously if the COOP $\rightarrow$0 then this procedure is useless as the angles will be inconsistent between the constructs. However, this procedure is a convenient way to determine the range in which it is most convenient to report the angle (i.e. $0\rightarrow\pi$ or $-\frac{\pi}{2}\rightarrow\frac{\pi}{2}$). Additionally, there are two possible angles that can be calculated (Fig. 2.1B). We chose to provide the clock-wise angle from $\overrightarrow{p}$ to $\overrightarrow{q}$, but it is also possible to calculate only the acute angle instead. To compare the COOP, COOP_c, and COOP_u in the analysis of the experimental data, the one way ANOVA with the Student-Newman-Keuls test was used.

2.3 Results

2.3.1 Theoretical Results

One of the main goals of this work was to develop a metric to quantify the correlation between the orientation of different biological constructs within the cell or tissue. In designing the new metric, we aimed to overcome the challenge of analyzing orientation of multiple pseudo vectors, i.e. the metric needed to be symmetric with the period of π for both vectors. The OOP was designed to analyze the organization of pseudo vectors, and has become a standard parameter for use in liquid crystals [31]. The OOP ranges from zero, for isotropic, to one, for aligned mediums (A.1), and it has been applied to various biological systems [75, 31, 34]. However, the OOP was not designed to evaluate the correlation of orientation of coupled constructs such as actin fibrils and Z-lines.The first step in creating the COOP was to formally define the problem. Let the first construct be P, a set of pseudo vectors $\overrightarrow{p_i}$, and the second construct be Q, a set of pseudo vectors $\overrightarrow{q_i}$ (Fig. 2.1A). The order tensor and

OOP of each field is:

$$\mathbb{T}_K = \left\langle 2 \begin{bmatrix} k_{i,x}k_{i,x} & k_{i,x}k_{i,y} \\ k_{i,x}k_{i,y} & k_{i,y}k_{i,y} \end{bmatrix} - \mathbb{I} \right\rangle = \{Mean\ order\ tensor\}, \tag{2.2}$$

$$OOP_K = \max\left[\text{eigenvalue}(\mathbb{T}_K)\right] = \{Orientational\ order\ parameter\ of\ K\}, \tag{2.3}$$

where $K = \{P, Q\}$, $\overrightarrow{k_i} = \{\overrightarrow{p_i}, \overrightarrow{q_i}\}$, and $\mathbb{I}$ is the identity matrix. To construct the new metric, we defined a new field F (a set of pseudo vectors $\overrightarrow{f_i}$):

$$f_{i,x} = \overrightarrow{p_i} \cdot \overrightarrow{q_i} = p_{i,x}q_{i,x} + p_{i,y}q_{i,y} = \cos(\theta)\ , \tag{2.4}$$

$$f_{i,y} = \left|\overrightarrow{p_i} \times \overrightarrow{q_i}\right| = p_{i,x}q_{i,y} - p_{i,y}q_{i,x} = \sin(\theta). \tag{2.5}$$

Physically, field F represent the angle (θ) between the two biological constructs, $\overrightarrow{p_i}$ and $\overrightarrow{q_i}$. The metric was then calculated similarly to the OOP:

$$\mathbb{T}_{PQ} = \left\langle 2 \begin{bmatrix} f_{i,x}f_{i,x} & f_{i,x}f_{i,y} \\ f_{i,x}f_{i,y} & f_{i,y}f_{i,y} \end{bmatrix} - \mathbb{I} \right\rangle = \{Mean\ tensor\ of\ the\ system\}. \tag{2.6}$$

$$\begin{aligned} COOP_{PQ} = \max\left[\text{eigenvalue}(\mathbb{T}_{PQ})\right] = &\{Co\text{-}orientational\ order \\ &parameter\ of\ the\ system\}\,. \end{aligned} \tag{2.7}$$

The analytical solution of the COOP is:

$$COOP_{PQ} = \left\langle 2\left\{\overrightarrow{f_i}\cdot\hat{n}\right\}^2 - 1\right\rangle = \left\langle 2\left\{\overrightarrow{f_i}\cdot\hat{n}\right\}^2\right\rangle - 1 = 2\left\langle\left\{\overrightarrow{f_i}\cdot\hat{n}\right\}^2\right\rangle - 1, \tag{2.8}$$

where $\hat{n}$, the director, is the eigenvector associated with the maximum eigenvalue of mean tensor $\mathbb{T}_{PQ}$. The director represents the mean angle between the two constructs. Alternatively, the COOP can be written in the expended form:

$$COOP_{PQ} = \langle f_{i,x}^2\rangle + \langle f_{i,y}^2\rangle - 1 + \sqrt{\left(\langle f_{i,x}^2\rangle - \langle f_{i,y}^2\rangle\right)^2 + 4\langle f_{i,x}f_{i,y}\rangle^2}. \tag{2.9}$$

The COOP was designed to range between zero and one. Here we present a series of theorems that illustrate the various properties of the COOP.

Theorem 1: Demonstration of COOP symmetry

Symmetry is an important characteristic of both the OOP and the COOP because it alleviates calculation errors that may arise when there is a random choice of signs for the pseudo vectors (Fig. 2.1B). Symmetry can be easily shown for OOP (A.2). As can be seen from the anyaltical solution of the COOP (Eq. 2.8), it is only necessary to demonstrate the symmetry of $\left\{\overrightarrow{f_i}\cdot\hat{n}\right\}^2$ in π to demonstrate the pseudo-symmetry of the COOP.

Table 2.1 shows the eight possible symmetry permutations. All of these can be reduced to the same equation with no difference in sign, which proves pseudo-vector symmetry of the COOP. We also demonstrated that the COOP is symmetric to the switch of P and Q:

$$f'_{i,x} = q_{i,x}p_{i,x} + q_{i,y}p_{i,y} = f_{i,x} \quad \text{and} \quad f'_{i,y} = q_{i,x}p_{i,y} - q_{i,y}p_{i,x} = -f_{i,y}, \tag{2.10}$$

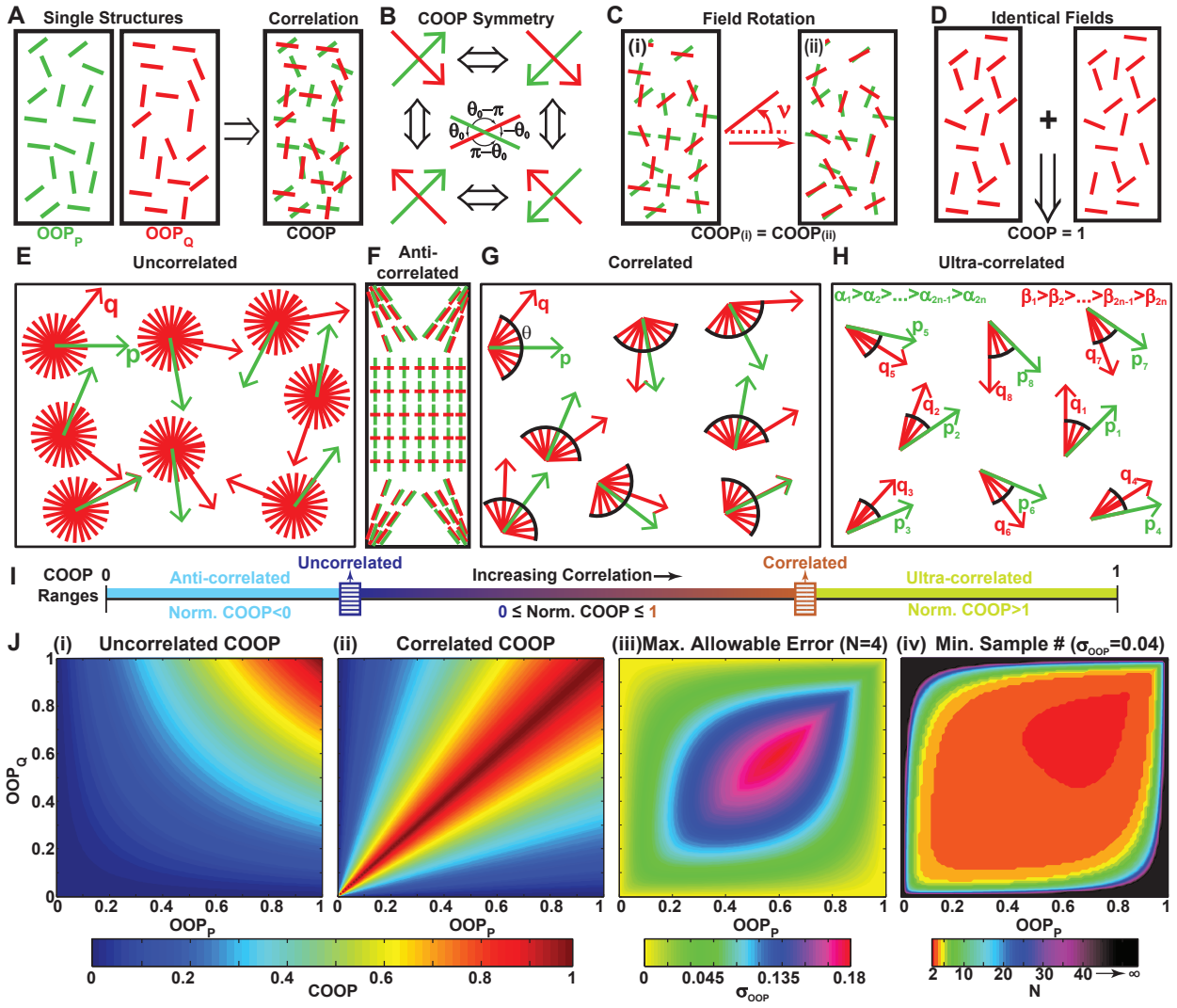

Figure 2.1: **Theoretical formulation of the co-orientational order parameter (COOP).**(A) The parameter is based on two independent sets of pseudo-vectors that are co-localized in space; (B) the COOP is symmetric to all permutations of 180° symmetry associated with the pseudo vectors; (C) the COOP remains the same if every pseudo-vector in one of the fields is rotated by the same angle; (D) if two identical fields of pseudo-vectors are compared to each other, $COOP = 1$; (E) The uncorrelated COOP graphically defined: $\overrightarrow{p}$ and $\overrightarrow{q}$ are completely independent of each other, thus a given $\overrightarrow{p}$ does not place any limits on the possible directions of $\overrightarrow{q}$; (F) Schematic example of two fields that are anti-correlated - parallel at the ends of the rectangle, yet perpendicular in the middle; (G) The correlated COOP graphically defined: for any $\overrightarrow{p}$, there exists a range of angles within which the $\overrightarrow{q}$ will be positioned; (H) The ultra-correlated case is similar to the correlated case, but there is also a global organization where the vectors are co-localized maximal angle to minimal angle; (I) Ranges of COOP and Normalized COOP defined on the top and bottom of the bar, respectively. The values of the uncorrelated and correlated COOP limits (sliders on image) are fully defined by the values of OOP_P and OOP_Q. If the $COOP_u>0$, the region between zero and $COOP_u$ corresponds to the anti-correlated arrangements. If $COOP_c<1$, the region between $COOP_c$ and one corresponds to the ultra-correlated arrangements; (J)(i) and (ii) $COOP_u$ and $COOP_c$ as a function of the OOP_P and OOP_Q respectively; (iii) Maximal allowable error in the OOP for there to be a statistically significant ($p<0.05$) difference between $COOP_u$ and $COOP_c$ if the sample size N=4. (iv) The minimum sample size, for statistical significance, with OOP error of $\sigma_{OOP} = 0.04$.

$$COOP_{QP} = \langle f_x^2 \rangle + \langle (-f_y)^2 \rangle - 1 + \sqrt{\left(\langle f_x^2 \rangle - \langle (-f_y)^2 \rangle \right)^2 + 4 \langle -f_x f_y \rangle^2} = COOP_{PQ}. \quad (2.11)$$

Symmetry also plays an important role in interpreting the COOP director. There are four valid results for an angles between two pseudo-vectors: θ_0, $-\theta_0$, $\pi - \theta_0$, $\theta_0 - \pi$ (Fig. 2.1B). For any symmetry permutation the director will correspond to one of these four angles. However, it is essential that the translation from $\hat{n}$ to θ_0 is handled with this symmetry in mind.

Table 2.1: **Symmetry Permutations**

$\overrightarrow{p_i}$	$\overrightarrow{q_i}$	$\hat{n}$	$\{\overrightarrow{f_i} \cdot \hat{n}\}^2$
+	+	+	$\{(p_{i,x}q_{i,x} + p_{i,y}q_{i,y})n_x + (p_{i,x}q_{i,y} - p_{i,y}q_{i,x})n_y\}^2 =$
+	+	-	$\{(p_{i,x}q_{i,x} + p_{i,y}q_{i,y})(-n_x) + (p_{i,x}q_{i,y} - p_{i,y}q_{i,x})(-n_y)\}^2 =$
+	-	+	$\{-(p_{i,x}q_{i,x} + p_{i,y}q_{i,y})n_x - (p_{i,x}q_{i,y} - p_{i,y}q_{i,x})n_y\}^2 =$
+	-	-	$\{-(p_{i,x}q_{i,x} + p_{i,y}q_{i,y})(-n_x) - (p_{i,x}q_{i,y} - p_{i,y}q_{i,x})(-n_y)\}^2 =$
-	+	+	$\{-(p_{i,x}q_{i,x} + p_{i,y}q_{i,y})n_x - (p_{i,x}q_{i,y} - p_{i,y}q_{i,x})n_y\}^2 =$
-	+	-	$\{-(p_{i,x}q_{i,x} + p_{i,y}q_{i,y})(-n_x) - (p_{i,x}q_{i,y} - p_{i,y}q_{i,x})(-n_y)\}^2 =$
-	-	+	$\{(p_{i,x}q_{i,x} + p_{i,y}q_{i,y})n_x + (p_{i,x}q_{i,y} - p_{i,y}q_{i,x})n_y\}^2 =$
-	-	-	$\{(p_{i,x}q_{i,x} +_{i,y} q_{i,y})(-n_x) + (p_{i,x}q_{i,y} - p_{i,y}q_{i,x})(-n_y)\}^2 =$
Result for All			$= \{(p_{i,x}q_{i,x} + p_{i,y}q_{i,y})n_x + (p_{i,x}q_{i,y} - p_{i,y}q_{i,x})n_y\}^2$

Theorem 2: Field rotation does not affect COOP

To verify that rotation of Q with respect to P does not affect COOP (Fig. 2.1C), let

$$\overrightarrow{p_i} = [\cos(\alpha), \sin(\alpha)] \quad \text{and} \quad \overrightarrow{q_i} = [\cos(\beta), \sin(\beta)]\,. \quad (2.12)$$

If each $\overrightarrow{q_i}$ was rotated by angle ν, the rotated field Q_{rot} would be defined by:

$$\begin{aligned}\overrightarrow{q}_{i,rot} &= [\cos(\beta+\nu), \sin(\beta+\nu)] \\ &= [\cos(\beta)\cos(\nu) - \sin(\beta)\sin(\nu), \sin(\beta)\cos(\nu) + \cos(\beta)\sin(\nu)]\,.\end{aligned} \tag{2.13}$$

Then the rotated field F_{rot} is:

$$\overrightarrow{f}_{i,rot} = [f_{i,x}\cos(\nu) - f_{i,y}\sin(\nu), f_{i,y}\cos(\nu) + f_{i,x}\sin(\nu)]. \tag{2.14}$$

As the angle ν is constant:

$$\begin{aligned}\langle f_{i,rot,x}\rangle &= \langle f_{i,x}\rangle\cos(\nu) - \langle f_{i,y}\rangle\sin(\nu) \quad \text{and} \\ \langle f_{i,rot,y}\rangle &= \langle f_{i,y}\rangle\cos(\nu) + \langle f_{i,x}\rangle\sin(\nu).\end{aligned} \tag{2.15}$$

In combining equations Eq. (2.14) and (2.9), all terms with ν cancel or are reduced to $\cos^2(\nu)+\sin^2(\nu) = 1$. As a result $COOP_{rot}$=COOP. Thus we have proven that field rotation does not affect COOP, and without loosing generality we can assume $\hat{n}_p = \hat{n}_q = [1, 0]$. This proves that the mean angle between fibers cannot be used to evaluate the correlation of orientations.

Theorem 3: The same field compared to itself gives COOP of 1

We next proved that the same field compared to itself would obtain a COOP of one (Fig. 2.1D). Imagine two sets of pseudo vectors distributed in a 2D space, $\overrightarrow{p_i}$ and $\overrightarrow{q_i}$. Let

$$\overrightarrow{p_i} = [\cos(\alpha), \sin(\alpha)]\,, \quad \text{and} \quad \overrightarrow{q_i} = [\cos(\alpha), \sin(\alpha)]\,. \tag{2.16}$$

Then, the field $\overrightarrow{f_i}$ of this system can be written as:

$$f_{i,x} = p_{i,x}q_{i,x} + p_{i,y}q_{i,y} = \cos^2(\alpha) + \sin^2(\alpha) = 1 \text{ and} \tag{2.17}$$

$$f_{i,y} = p_{i,x}q_{i,y} - p_{i,y}q_{i,x} = \cos(\alpha)\sin(\alpha) - \sin(\alpha)\cos(\alpha) = 0. \tag{2.18}$$

The mean tensor:

$$\mathbb{T}_{PQ} = \left\langle 2 \begin{bmatrix} f_{i,x}f_{i,x} & f_{i,x}f_{i,y} \\ f_{i,x}f_{i,y} & f_{i,y}f_{i,y} \end{bmatrix} - \mathbb{I} \right\rangle = \left\langle 2 \begin{bmatrix} 1 & 0 \\ 0 & 0 \end{bmatrix} - \mathbb{I} \right\rangle = \begin{bmatrix} 1 & 0 \\ 0 & -1 \end{bmatrix}. \tag{2.19}$$

Therefore, the COOP of constructs P and Q:

$$COOP_{PQ} = \max \left[\text{eigenvalue} \left(\begin{bmatrix} 1 & 0 \\ 0 & -1 \end{bmatrix} \right) \right] = 1. \tag{2.20}$$

We obtained a COOP of 1 thus constructs P and Q are a perfectly co-oriented system which is expected as $P = Q$.

Theorem 4: Uncorrelated COOP Limit

For any given pair of fields with OOP_P and OOP_Q there is a range of possible COOP values, with a maximum range of zero to one. To aid in interpreting the meaning of the COOP, we derived the value for the COOP (COOP_u) as a function of the OOPs for the maximally uncorrelated system. For the COOP to be uncorrelated the two fields needed to have no correlation between their orientations (Fig. 2.1E). If and only if $\overrightarrow{p_i}$ and $\overrightarrow{q_i}$ are assumed independent and $\hat{n}_p = \hat{n}_q$ (Theorem 2), the analytical solution Eq. (2.8) can be re-written

as:

$$COOP_u = \Big\langle 2(p_{i,x}q_{i,x} + p_{i,y}q_{i,y})^2 - 1 \Big\rangle = \Big\langle (2p_{i,x}^2 - 1)(2q_{i,x}^2 - 1) \Big\rangle. \tag{2.21}$$

Using the classical probability distribution property:

$$COOP_u = \Big\langle (2p_{i,x}^2 - 1)(2q_{i,x}^2 - 1) \Big\rangle = \Big\langle (2p_{i,x}^2 - 1) \Big\rangle \Big\langle (2q_{i,x}^2 - 1) \Big\rangle. \tag{2.22}$$

Based on the definition of the OOP the uncorrelated COOP is:

$$COOP_u = \Big\langle (2p_{i,x}^2 - 1) \Big\rangle \Big\langle (2q_{i,x}^2 - 1) \Big\rangle = OOP_P OOP_Q = \{Uncorrelated\ COOP\}. \tag{2.23}$$

$\mathrm{COOP_u}$ is the lowest limit of the COOP if and only if the two constructs are independent. However, if P and Q are correlated in multiple ways it is possible to achieve a smaller value of COOP.

Theorem 5: Anti-correlated COOP

To prove that $\mathrm{COOP_u}$ is not necessarily the minimum COOP, we constructed an example where P was composed of $\overrightarrow{p_1}$ and $\overrightarrow{p_2}$, and construct Q was composed of $\overrightarrow{q_1}$ and $\overrightarrow{q_2}$:

$$\overrightarrow{p_1} = [\cos(\alpha), \sin(\alpha)] \quad \text{and} \quad \overrightarrow{p_2} = [\cos(-\alpha), \sin(-\alpha)]\,. \tag{2.24}$$

$$\overrightarrow{q_1} = \Big[\cos(\alpha + \frac{\pi}{2}), \sin(\alpha + \frac{\pi}{2})\Big] \quad \text{and} \quad \overrightarrow{q_2} = [\cos(-\alpha), \sin(-\alpha)]\,. \tag{2.25}$$

Construct P has an $OOP_{\mathrm{P}} = \cos(2\alpha)$ and construct Q has an $OOP_{\mathrm{Q}} = |\sin(2\alpha)|$. The vector $\overrightarrow{f}$ is:

$$f_{1,x} = 0 \ , \ f_{2,x} = 1 \text{ and } f_{1,y} = 1 \ , \ f_{2,y} = 0. \tag{2.26}$$

The mean tensor and COOP of this system are:

$$\mathbb{T}_{PQ} = \begin{bmatrix} 0 & 0 \\ 0 & 0 \end{bmatrix} \text{ and } COOP = 0. \tag{2.27}$$

Using Eq. (2.23) we obtained:

$$COOP_u = OOP_P \cdot OOP_Q = \cos(2\alpha)\,|\sin(2\alpha)|\,. \tag{2.28}$$

Unless, $\alpha \neq \{0, \frac{\pi}{4}, \frac{\pi}{2}\} \cdot n$ for $n = \{1, 2, \dots\}$, $\mathrm{COOP_u}$>0. Thus, the COOP can be lower than $\mathrm{COOP_u}$. Such a case can be graphically imagined if you have constructs correlated in two different ways in the same cell (Fig. 2.1F), similar to a single cardiomyocyte with punctate alpha-actinin at the ends and well defined Z-lines in the middle. This demonstrates that, similarly to the OOP, the COOP will not fully capture second order correlations (A.3).

Theorem 6: Correlated COOP Limit

For the upper limit, we derived the value of the COOP as a function of the OOPs for the maximally correlated constructs. To determine the correlated COOP ($\mathrm{COOP_c}$), we assumed the two fields, P and Q, were almost identical, except that Q was rotated by a random noise angle θ (Fig. 2.1G). We can assume, without loosing generality, $\hat{n}_p = \hat{n}_q = [1, 0]$ (Theorem 2), and P is better organized (i.e. $\mathrm{OOP_P}$>$\mathrm{OOP_Q}$, Theorem 1). Using the analytical solutions,

the OOP_P and COOP were rewritten as:

$$OOP_P = \Big\langle 2\cos^2(\alpha) - 1 \Big\rangle \quad \text{and} \quad COOP = \Big\langle 2\cos^2(\theta) - 1 \Big\rangle. \tag{2.29}$$

As θ was assumed to be random noise generated, θ and α are independent, and therefore:

$$\begin{aligned} OOP_Q &= \Big\langle 2\cos^2(\alpha-\theta) - 1 \Big\rangle \\ &= \Big\langle (2\cos^2(\alpha) - 1)(2\cos^2(\theta) - 1) + 4\cos(\alpha)\sin(\alpha)\cos(\theta)\sin(\theta) \Big\rangle \\ &= \Big\langle (2\cos^2(\alpha) - 1)(2\cos^2(\theta) - 1) \Big\rangle + \Big\langle 2\cos(\alpha)\sin(\alpha) \Big\rangle \Big\langle 2\cos(\theta)\sin(\theta) \Big\rangle \\ &= \Big\langle (2\cos^2(\alpha) - 1) \Big\rangle \Big\langle (2\cos^2(\theta) - 1) \Big\rangle + \Big\langle \sin(2\alpha) \Big\rangle \Big\langle \sin(2\theta) \Big\rangle \\ &= OOP_P COOP_c. \end{aligned} \tag{2.30}$$

Solving for $COOP_c$ and rewriting it in a more general form we obtained:

$$COOP_c = \frac{min(OOP_P, OOP_Q)}{max(OOP_P, OOP_Q)}. \tag{2.31}$$

This is the upper limit of COOP if the two constructs are correlated but are subject to random biological variance (noise). This would not be the limit in a system where the variance is not random.

Theorem 7: Ultra-correlated COOP

We also showed that the correlated COOP is not necessarily the maximum. To prove this we defined P and Q as:

$$\overrightarrow{p_i} = [\cos(\alpha_i), \sin(\alpha_i)] \text{ and } \overrightarrow{p}_{n+i} = [\cos(-\alpha_i), \sin(-\alpha_i)] \tag{2.32}$$

$$\overrightarrow{q_i} = [\cos(\alpha_i + \theta_i), \sin(\alpha_i + \theta_i)] \text{ and } \overrightarrow{q}_{n+i} = [\cos(-\alpha_i - \theta_i), \sin(-\alpha_i - \theta_i)] \tag{2.33}$$

for $i = \{1, ..., n\}$. Thus, each set of angles is paired in decreasing order (Fig. 2.1H). $\mathrm{OOP_P}$ and $\mathrm{OOP_Q}$ are defined as:

$$OOP_P = \frac{1}{n}\sum_{i=1}^{n}\cos(2\alpha_i) \text{ where } \alpha_i : \sum_{i=1}^{n}\cos(2\alpha_i) \geq 0 \tag{2.34}$$

$$OOP_Q = \frac{1}{n}\sum_{i=1}^{n}\cos(2\alpha_i + 2\theta_i) \text{ where } \alpha_i, \theta_i : \sum_{i=1}^{n}\cos(2\alpha_i + 2\theta_i) \geq 0. \tag{2.35}$$

Assuming $\sum_{i=1}^{n}\cos(2\theta_i) \geq 0$ the mean tensor is:

$$\mathbb{T}_{PQ} = \begin{bmatrix} \frac{2}{n}\sum_{i=1}^{n}\cos^2(\theta_i) & 0 \\ 0 & -\frac{1}{n}\sum_{i=1}^{n}(2\cos^2(\theta_i) - 2) \end{bmatrix}. \tag{2.36}$$

Knowing $COOP = \frac{1}{n}\sum_{i=1}^{n}\cos(2\theta_i)$ and the $\mathrm{COOP_c}$=$\frac{OOP_Q}{OOP_P}$:

$$COOP - COOP_c = \frac{1}{n}\sum_{i=1}^{n}\cos(2\theta_i) - \frac{\sum_{i=1}^{n}\cos(2\alpha_i + 2\theta_i)}{\sum_{i=1}^{n}\cos(2\alpha_i)}. \tag{2.37}$$

If the expression in Eq. (2.37) is positive, then $COOP \geq COOP_c$. An example of such a case is when θ is constant and Eq. (2.37) becomes:

$$COOP - COOP_c = \frac{\sum_{i=1}^{n} \sin(2\alpha_i)\sin(2\theta_i)}{\sum_{i=1}^{n} \cos(2\alpha_i)}. \tag{2.38}$$

Based on conditions in Eq. (2.34) and (2.35), $0 \leq \alpha_i \leq \frac{\pi}{2}$ and $0 \leq \theta_i \leq \frac{\pi}{2}$, which implies $\sin(2\alpha_i) \geq 0$, $\cos(2\alpha_i) \geq 0$, and $\sin(2\theta_i) \geq 0$ for all i. Therefore, every term in Eq. (2.38) is positive. If P is not perfectly aligned (i.e. $\alpha_i \neq 0$), and if P and Q are not identical (i.e. $\theta_i \neq 0$), then COOP>COOP_c. Thus, there is an ultra-correlated COOP that can be greater than $COOP_c$. Qualitatively, the ultra-correlated system is similar to the correlated example, except the $\overrightarrow{q}$ vectors are not random within the noise, but are arranged maximum to minimum angles (Fig. 2.1H).

Normalized COOP

Based on Theorems 4-7 we can divide the range of COOP into three regions (Fig. 2.1I): anti-correlated, normal, and ultra-correlated. The boundaries of these regions (COOP_u and COOP_c) are determined by the organization of the two constructs (OOP_p and OOP_q) and will slide along the overall range [0,1]. Experimentally, it might be more relevant to know how close the COOP is to the uncorrelated and correlated boundaries as these carry biological implications. We therefore defined a Normalized COOP, which is a measure of how close a parameter is to COOP_u or COOP_c:

$$\text{Normalized COOP} = \frac{COOP - COOP_u}{COOP_c - COOP_u}. \tag{2.39}$$

The normalized COOP is negative when it is anti-correlated, zero when the system is uncorrelated, one when it is correlated, and greater than one when it is ultra-correlated

(Fig. 2.1I). Any parameter has limitations. For example, the OOP of the red line-segments in the anti-correlated schematic (Fig. 2.1F) would be equivalent to an isotropic organization ($OOP \sim 0$) even though the red line-segments are well organized. Similarly, the COOP cannot be used to identify correlations in tissues that have very non-trivial spatially dependent correlations (more complex than the ultra-correlated case (Fig. 2.1H)). We believe that most biological constructs for which the COOP has been developed will never exhibit this behavior. However, if the COOP is ever found to be statistically significantly greater than $\mathrm{COOP_c}$, it will be essential to re-evaluate the applicability of the parameter.

Estimated maximum tolerable error and minimum sample size

To interpret the information provided by the COOP, we would need to know which region our tissue falls under. Our ability to do so will be limited by the error inherent in any measurement and the width of the normal COOP range. $\mathrm{COOP_u}$ approaches the maximum ($\mathrm{COOP_u}$=1) as both $\mathrm{OOP_p}$ and $\mathrm{OOP_q}$ approach one (Fig. 2.1J(i)). $\mathrm{COOP_c}$, however, approaches its maximum when the two order parameters are close to being equal (Fig. 2.1J(ii)). This shows, for example, that if $\mathrm{OOP_p}$=0 and $\mathrm{OOP_q}$=0, then the normal region of the COOP ranges [0,1]. However, if $\mathrm{OOP_p}$>0 and $\mathrm{OOP_q}$=0, the normal range does not exist and a COOP>0 would indicate an ultra-correlated system. If the error in the system is so large that there is no statistically significant difference between the boundaries ($\mathrm{COOP_u}$ and $\mathrm{COOP_c}$), it would not be possible to differentiate between the regions. Therefore, for the parameter to be useful, the maximum allowable error and minimum sample size have to be experimentally realistic. To estimate the error and sample size, we calculated the propagation of error in $\mathrm{COOP_u}$ and $\mathrm{COOP_c}$, and used them in the student t-test to calculate statistical significance.

Assuming $\mathrm{OOP_P}$ and $\mathrm{OOP_Q}$ are normally distributed with the standard deviation σ_{OOP_P}

and $\sigma_{OOP_{\mathrm{Q}}}$, respectively, and $\mathrm{OOP_P}$ and $\mathrm{OOP_Q}$ are independent, then the variance:

$$\begin{aligned}\sigma^2_{COOP_u} &= \left(\frac{\partial COOP_u}{\partial OOP_P}\right)^2 \sigma^2_{OOP_P} + \left(\frac{\partial COOP_u}{\partial OOP_Q}\right)^2 \sigma^2_{OOP_Q} \\ &= OOP_Q^2 \sigma^2_{OOP_P} + OOP_P^2 \sigma^2_{OOP_Q},\end{aligned} \tag{2.40}$$

and the standard deviation:

$$\sigma_{COOP_u} = \sqrt{OOP_Q^2 \sigma^2_{OOP_P} + OOP_P^2 \sigma^2_{OOP_Q}}. \tag{2.41}$$

Assuming $\mathrm{OOP_P}$>$\mathrm{OOP_Q}$, the variance for the correlated COOP:

$$\begin{aligned}\sigma^2_{COOP_c} &= \left(\frac{\partial COOP_c}{\partial OOP_P}\right)^2 \sigma^2_{OOP_P} + \left(\frac{\partial COOP_c}{\partial OOP_Q}\right)^2 \sigma^2_{OOP_Q} \\ &= \left(\frac{OOP_Q}{OOP_P^2}\right)^2 \sigma^2_{OOP_P} + \left(\frac{1}{OOP_P}\right)^2 \sigma^2_{OOP_Q}.\end{aligned} \tag{2.42}$$

Note that $\frac{\partial COOP_{\mathrm{c}}}{\partial OOP_{\mathrm{P}}}$ and $\frac{\partial COOP_{\mathrm{c}}}{\partial OOP_{\mathrm{Q}}}^2$ do not exist when $\mathrm{OOP_P}$=$\mathrm{OOP_Q}$. However, using Theorem 1, we formulated the estimate for the the standard deviation of $\mathrm{COOP_c}$:

$$\sigma_{COOP_c} = \begin{cases} \sqrt{\left(\frac{OOP_Q}{OOP_P^2}\right)^2 \sigma^2_{OOP_P} + \left(\frac{1}{OOP_P}\right)^2 \sigma^2_{OOP_Q}} & : OOP_P > OOP_Q \\ \sqrt{\left(\frac{1}{OOP_Q}\right)^2 \sigma^2_{OOP_P} + \left(\frac{OOP_P}{OOP_Q^2}\right)^2 \sigma^2_{OOP_Q}} & : OOP_P < OOP_Q. \end{cases} \tag{2.43}$$

Then to estimate maximum allowable error, we assumed $\sigma_{OOP_{\mathrm{P}}} = \sigma_{OOP_{\mathrm{Q}}}$, and tested the null hypothesis of $\mathrm{COOP_u}$=$\mathrm{COOP_c}$. We calculated the t-value and degrees of freedom to complete the t-test. We assumed significance for a p-value less than 0.05 for the two sample t-test. There are two variables that impact significance as a function of OOPs: the error (σ_{OOP}) and the sample size (N). For visualization, we calculated the maximum allowable experimental error ($max(\sigma_{OOP})$) at sample size of four (Fig. 2.1J(iii)). The maximal allowable error at N=4 was at its highest, $max(\sigma_{OOP}) = 0.18$, for $\mathrm{OOP_P}$=$\mathrm{OOP_Q}$=0.60,

which is greater than experimental error reported for OOP organization [24]. While the maximal allowable error approaches zero as OOP→0, it rapidly increases for OOP>0.

We also determined the minimum sample size that provides statistical significance ($p<0.05$) as a function of construct organization for $\sigma_{OOP} = 0.04$. The minimum sample size ranges from two to infinity (Fig. 2.1J(iv)). Naturally, when $COOP_c \rightarrow COOP_u$, the $min(N) \rightarrow \infty$ as it is not possible to find them significantly different. For $\sigma_{OOP} = 0.04$, the minimum sample size is between two and five for most of the OOP values. For convenience, we also calculated the minimum sample size for a range of higher experimental errors (Fig. A.2). Obviously higher error would necessitate more samples to maintain significance. However, errors reported for OOP experimentally correspond to normal requirements in sample size. The errors and sample sizes were confirmed to be experimentally realistic, thus we next moved to testing the parameter with synthetic and experimental data.

2.3.2 Synthetic Results

Limiting cases

The first step to validate the new parameter was to construct four limiting cases that should lead to specific COOP values. We constructed a custom MatLab code that could be interfaced with experimental or synthetic (computer generated) data. The code was used to confirm the COOP for four synthetic limiting cases. The first test was to compare two perfectly aligned constructs (Fig. 2.2A(i)). It was clear from the image that these two constructs were perfectly correlated, and we therefore expected COOP=1. We first confirmed that both constructs were perfectly aligned with $OOP_P=OOP_Q=1$ (Fig. 2.2A(ii)). Analytically, it is clear that COOP=1, by first applying Theorem 2 and then Theorem 3. When the synthetic data for this condition was analyzed by the code, the COOP was confirmed to be one (Fig. 2.2A(iii)). It is worthwhile to note that the director

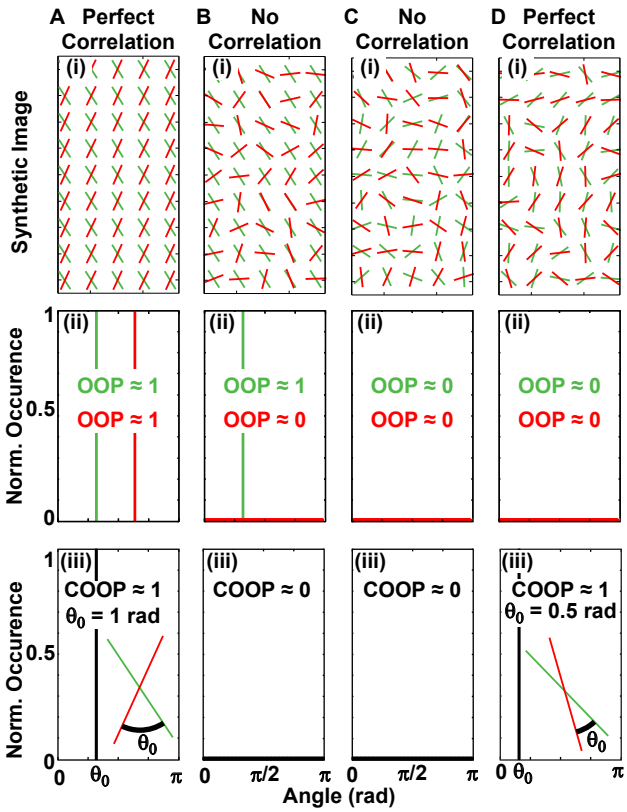

Figure 2.2: **Synthetic data for four limiting cases.** (A) Two perfectly organized samples are always perfectly correlated; (B) A perfectly organized and an isotropic construct cannot be correlated; Two isotropic cases can be (C) completely uncorrelated and (D) perfectly correlated. For (A-D) (i) Schematic of a small section of the synthetic data; (ii) OOP and normalized occurrence for both constructs; (iii) COOP results with θ_0 designating the mean angle between constructs.

generated by the COOP code corresponds to the angle, θ_0, between the constructs.

For the second limiting condition, one construct was perfectly organized, while the second was completely disorganized (Fig. 2.2B(i)). In this case, there was no correlation, and we expected COOP=0. Analytically, even if we supposed that the two constructs were maximally correlated (COOP=COOP_c) and applied Theorem 6 based on OOP_Q=1 and OOP_P=0 (Fig. 2.2B(ii)), the COOP=0. This was confirmed by the result of the synthetic case (Fig. 2.2B(iii)).

The third case considered two isotropic constructs that are completely uncorrelated (Fig. 2.2C(i)-(ii)). We expected the COOP for uncorrelated constructs to be zero, and

analytically this was confirmed by Theorem 4. These findings were also confirmed by the results of the synthetic data (Fig. 2.2C(iii)).

The fourth, most intriguing case, was of two isotropic constructs, which were perfectly correlated (Fig. 2.2D(i)-(ii)). We expected the COOP to be one as there was perfect correlation, and this was proven by Theorem 6. Synthetically we showed the COOP=1, and again the director gave the average angle, θ_0, between constructs. The limiting conditions validated the parameter for four simple cases. However, the interpretation of the COOP gets more complex when neither construct is perfectly aligned or isotropic.

$\mathbf{COOP_u}$ and $\mathbf{COOP_c}$ demonstrated with synthetic data

To understand the limits of the COOP parameter, we constructed a series of cases with different organizations by truncation of Gaussian distributions with specified standard deviations (Fig. 2.3A and 2.3B). We created synthetic data for the uncorrelated case (dark blue Fig. 2.3C) by generating two separate random number sets using the appropriate truncated Gaussian distribution for each. For the correlated case (brown Fig. 2.3C), we generated the first, more organized, data set by the same method. Then the noise was generated such that when it was added to the first data set, the new set would have the target distribution. Both methods of creating P and Q data sets lead to the same desired individual distributions (Fig. 2.3A and 2.3B). To visualize the results we constructed a slider, sketched in Fig. 2.1I, for each case (Fig. 2.3C) color-coded to indicate the boundaries, $\mathrm{COOP_u}$ (dark blue) and $\mathrm{COOP_c}$ (brown), as well as the three regions: anti-correlated (light blue), normal (ranging from dark blue to brown), and ultra-correlated (bright green). We expected that when $\mathrm{OOP_P}$=1 (Fig. 2.3A(i)), $\mathrm{COOP_u}$=$\mathrm{COOP_c}$=$\mathrm{OOP_Q}$ for all $\mathrm{OOP_Q}$ values, which was confirmed by the results of the synthetic data (Fig. 2.3C(i)-(iii)). Also, if one OOP=0 (Fig. 2.3B(i)) and the other $OOP \neq 0$, the $\mathrm{COOP_u}$=$\mathrm{COOP_c}$=0. This was also confirmed with synthetic results (Fig. 2.3C(i) and

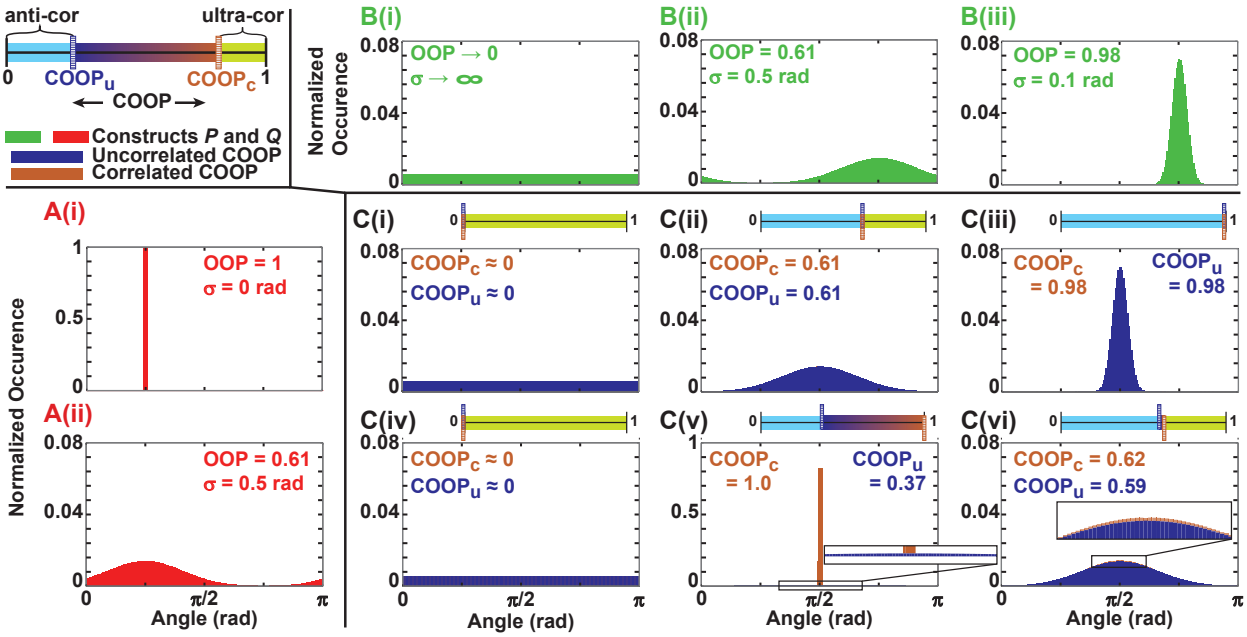

Figure 2.3: **Boundaries of normal region of the COOP.**(A and B) The orientation distribution for construct A and B respectively with both the standard deviation of the truncated Gaussian distribution and OOP indicated for each case; (C) the distribution of the angles between the two constructs if they are independent of each other (dark blue) and if the difference is dictated by a random noise (brown). For each case the boundaries, $\mathrm{COOP_u}$ and $\mathrm{COOP_c}$, are indicated. Sliders show this graphically with regions colored according to the legend.

2.3C(iv)). For a case where $OOP \neq \{0 \text{ or } 1\}$ the normal range of the COOP was greater if the OOPs were smaller and closer to each other, which can be seen by comparing Fig. 2.3C(v) and Fig. 2.3C(vi). These synthetic results confirm the results of Fig. 2.1, which showed that the COOP parameter is best applied in situations where the correlation is not obviously dictated by the organization of the individual constructs.

2.3.3 Experimental Results

The COOP was designed as a tool to evaluate correlations of orientation in experimental samples. We used actin fibers and sarcomeric Z-lines in NRVMs to validate the parameter and code. The tissues were stained for α-actinin and phalloidin to identify Z-line and actin

fibril directions, respectively (Fig. 2.4A). The program we used to identify the direction of the construct was based on a finger-print identification code [38, 46, 10], and it assigned a direction to every non-empty pixel in the image. However, computing correlation of constructs based on individual pixels introduced too many errors. Indeed, most images of cytoskeleton constructs are obtained via immunostaining and imaging. The accuracy of the COOP will be a direct consequence of image quality. If the images are of poor quality (poor contrast, dead cells, etc.), it will not be possible to accurately extract the construct direction data, and thus, the COOP will not be accurate. However, if it is possible to accurately extract directionality data, the COOP can be used. The images we have collected for the proof-of-principle data set are representative of the images normally used to study tissue architecture [10, 31]. The images may be resolvable to different degrees, and image acquisition procedures can introduce inaccuracies at smaller scales. For example, during the collection of this data, it is customary to ensure that each channel results in sharp images of the corresponding construct, such as actin and Z-lines. This sometimes requires focusing on slightly different planes, and as a result, the images of the same field-of-view could be slightly off-set from each other. This along with other imaging inaccuracies lead us to develop a procedure to average out these small errors by calculating the direction of each construct within grid-squares. While any consistent small grid can be used for comparing results across multiple tissues, we recommend picking a grid size that would correspond to a natural biological unit. In this case, the image was partitioned into a grid (Fig. 2.4B), which was chosen such that at minimum, two Z-lines could be expected to fit within each grid-square, ensuring that at least one "sarcomere" complex is within each square (Fig. A.3). The spacing between Z-lines in NRVM tissues is 1.9-2.1 µm[30], thus we chose a grid size close to 4.2 µm (∼30 pixels). For each grid (i), we calculated the average direction for both constructs (i.e. Z-lines or actin fibrils) (Fig. 2.4C). To account for varying densities and partial grid-squares at the edges of the images, the area density (ρ) was calculated for each grid-square using the number of non zero angles in the

grid-square divided by its area. Each grid-square (i) was assigned a weight (W_i) based on the OOP and density of constructs (ρ):

$$W_i = OOP_{P,i} \cdot OOP_{Q,i} \cdot \rho_{P,i} \cdot \rho_{Q,i}. \tag{2.44}$$

Thus, partial grids with low densities have small weight factors whereas full grids have high weight factors (length of arrows in Fig. 2.4D). Additionally, grid-squares with better alignment have higher weights than grid-squares with isotropic organization, which prevents loss of consistency.

Z-lines and actin fibers were expected to be perfectly correlated within the sarcomeres of the healthy cardiac muscle tissue. However, histological samples may not be perfect, with some example imperfections identified in the zoomed-in image of Fig. 2.4C, which correspond to the non-perpendicular arrows identified in Fig. 2.4D. Note that the lengths of the arrows correspond to the weights assigned to each square, so these imperfections can significantly alter the resulting COOP. To test the parameter, we took four coverslips with 10 fields of view imaged for each and identified noiseless regions with minimal imperfections (Fig. 2.4E-F). Before any angle detection was done, ImageJ was used to merge fields of view containing Z-lines and actin fibrils, and regions with minimal imperfections were chosen by an experienced user. Only merged images that contained four or more regions of minimal imperfections were used (Fig. 2.4E). This was done prior to the organizational analysis to eliminate bias. The implementation of the code is summarized in a flow chart (Fig. A.4).

The OOPs for actin fibrils and Z-lines were essentially the same for both the raw and masked images. We measured no significant difference in the values of $\mathrm{COOP_u}$ or $\mathrm{COOP_c}$ between the full and noiseless data sets (Fig. 2.4G). There was also no significant difference between COOP and $\mathrm{COOP_c}$ for the masked, noiseless images. In contrast there was a significant difference between COOP and $\mathrm{COOP_c}$ ($p<0.001$) for the raw images. This is reflected in

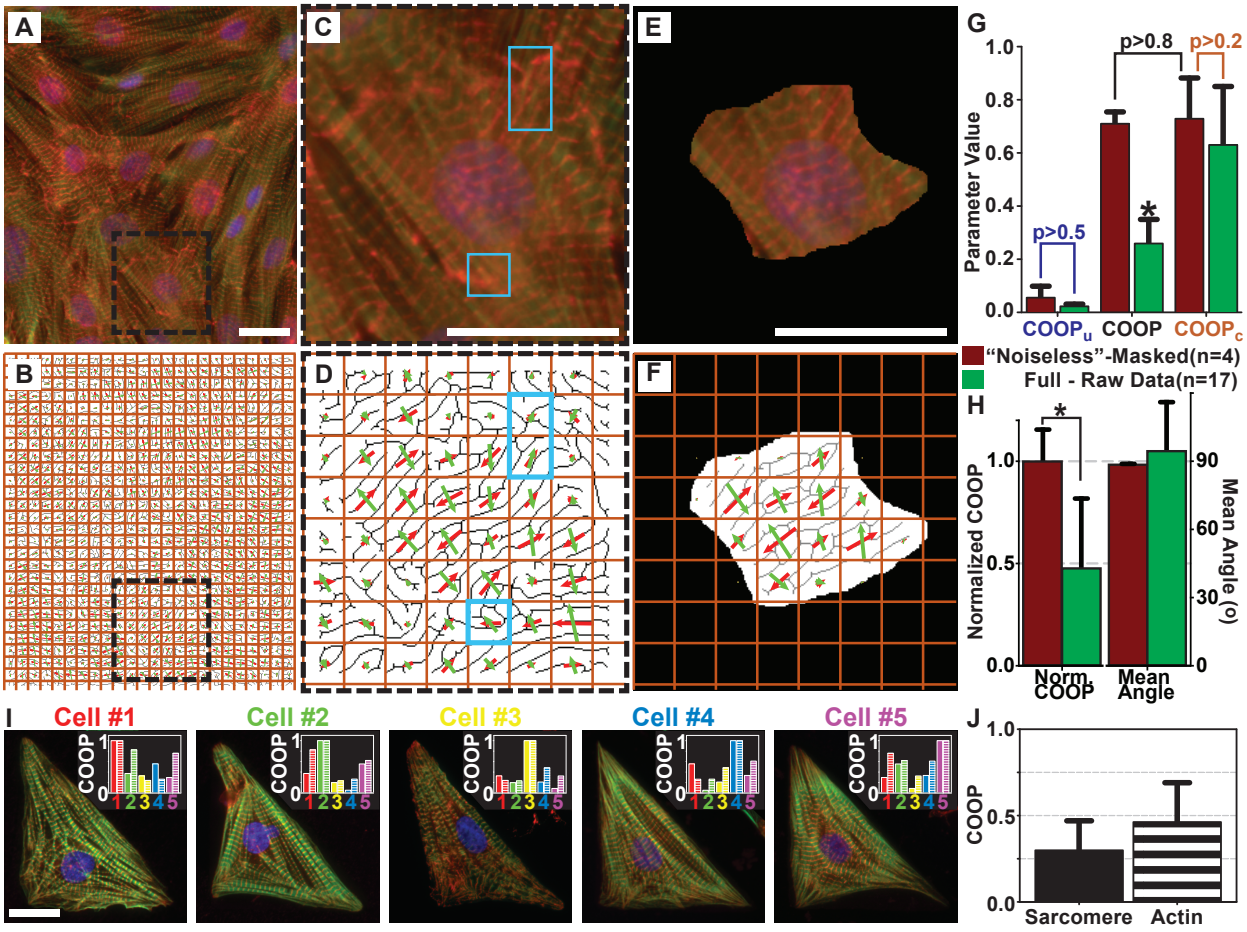

Figure 2.4: **Experimental applications of the COOP.** (A) Stained isotropic monolayer of NRVMs; (B) the grid used to calculate average Z-line and actin fibrils direction overlaid on the Z-line skeleton. (C) A section of the stained isotropic NRVM monolayer shown at a higher magnification (corresponds to the dashed box in A). Blue boxes point to some imperfections in the tissue and/or staining with clumps of α-actinin. (D) The skeletonized Z-lines from the image in (C) overlaid with the direction of actin fibrils (green arrows) and sarcomere z disks (red arrows) for every grid-square. Note that arrows in blue boxes are not perpendicular. (E) The image from (C) masked to only show noiseless tissue. (F) The actin fibril and Z-line directions overlaid on the Z-line skeleton from (E). (G) COOP$_u$, COOP, and COOP$_c$ for noiseless and raw images, (*) indicates statistical significance of $p<0.001$ between the raw COOP and raw COOP$_c$. (H) Normalized COOP and mean angle (clockwise from actin fibril to Z-line) for raw and noiseless images. (I) NRVMs cultured on identical FN islands. Each image contains a histogram of COOP between that cell and all others (solid-Z-line, stripe-actin fibril). (J) The average COOP for consistency of Z-line (solid) and actin fibril (stripe) organization. For (A), (C), (E), and (I) stains are: green - actin, red - α-actinin, and blue - nuclei. For (G), (H), and (J), error bars represent standard deviation. The n indicates the number of cover-slips, with at least 10 field of view taken for each. Scale bars = 20µm.

the Normalized COOP which is 1 for the noiseless images and less than 0.5 for the full data (Fig. 2.4H). This illustrates that while the parameter is capable of capturing the expected correlation in a sarcomere between actin fibril and Z-line orientation, cardiac tissues may have imperfections that result in a lower value of COOP. The mean angle for the noiseless images also shows the expected perpendicular correlation between orientations of sarcomere Z-lines and actin fibrils with minimal error (Fig. 2.4H). While, they were also approximately perpendicular in the raw images, the error was greater than for the noiseless images.

The COOP can also be used to evaluate the consistency of construct orientation within cells of the same shape. As an example we seeded NRVMs on triangular islands, and stained the samples for nucleus, Z-lines, actin fibrils, and fibronectin (Fig. 2.4I). For analysis we ensured that the fibronectin islands lined up for all five cells (A.5). Then the Z-line (solid bars) or actin fibril (dashed bars) images were compared in a pairwise manner (Tables 2.2 and 2.3). This showed an additional experimental confirmation of Theorem 3: COOP=1 for each cell when it was compared with itself (Fig. 2.4I). The COOP was calculated for the same grid as in the isotropic images. The results showed that although there is an overall consistency between cells, i.e., myofibrils were bundled along the edges of the triangle, the orientation was not fully consistent at a smaller length scale (grid size). Indeed, the average COOP for ten pair-wise comparisons (bold in Tables 2.2 and 2.3) of both Z-lines and actin fibrils is less than 0.5 (Fig. 2.4K). This demonstrated another potential use of this parameter.

Table 2.2: **Pairwise comparison of sarcomeric Z-lines consistency**

$COOP_{sarc}$	Cell 1	Cell 2	Cell 3	Cell 4	Cell 5
Cell 1	1.00	**0.37**	**0.33**	**0.56**	**0.30**
Cell 2	0.37	1.00	**0.20**	**0.05**	**0.55**
Cell 3	0.33	0.20	1.00	**0.21**	**0.09**
Cell 4	0.56	0.05	0.21	1.00	**0.34**
Cell 5	0.30	0.55	0.09	0.34	1.00

Table 2.3: **Pairwise comparison of actin fibrils consistency**

$COOP_{actin}$	Cell 1	Cell 2	Cell 3	Cell 4	Cell 5
Cell 1	1.00	**0.83**	**0.24**	**0.26**	**0.76**
Cell 2	0.83	1.00	**0.23**	**0.26**	**0.62**
Cell 3	0.24	0.23	1.00	**0.48**	**0.33**
Cell 4	0.26	0.26	0.48	1.00	**0.61**
Cell 5	0.76	0.62	0.33	0.61	1.00

2.4 Discussion

Colocalization, a process that analyzes the spatial overlap between two biological constructs, has been key in discovering cellular mechanisms that rely on the proximity of constructs [71, 74]. For example, second-order stereology has been used to analyze spatial arrangements of constructs in images. Noorafshan et al. used second-order stereology to examine the correlation between the spatial arrangements of cardiomyocytes and microvessels [54]. Their method involved pair correlation and cross-correlation functions to determine positive or negative correlation at different distances. However, neither simple colocalization nor second-order stereology do not analyze the relative orientations of biological constructs.

In this work, we have developed a new parameter, COOP, to characterize how two tissue components align with respect to each other. The COOP would allow for investigation of mechanisms or functions that rely on not only spatial proximity, but also specific organizational schemes. To properly interpret the meaning of the parameter values, we characterized it through a series of analytical theorems. As a result, we defined three regimes – normal, ultra-correlated, and anti-correlated – that have biological implications. After validating the parameter with synthetic data, we demonstrated its use with experimental images by showing that perfect portions of cardiac tissues have the expected correlation of the orientation between sarcomeric z-discs and actin fibrils. The reduction in

the COOP for un-masked (raw) data suggests that the defects in the architecture will be distinguished by our new method (Fig. 2.4G-H). The code we have developed can also be used to calculate the mean angle between constructs thus allowing for tracking of mean angle changes as a function of experimental conditions. Furthermore, the parameter can be used to calculate the consistency of orientational organization to help evaluate the importance of orientational order.

To compare organization between different experimental conditions, it is necessary to have a robust metric. The best metrics place the least number of constraints on the distribution of orientations. For example, the standard deviation is not an appropriate metric for quantifying orientation distribution of Z-lines as they are not distributed normally. The OOP works with all types of distributions, and it has an additional benefit of being symmetric to pseudo-vectors [34]. As the COOP was designed with similar math, it shares the same benefits as the OOP such as pseudo-vector symmetry.

In general, there are multiple ways to use mathematical functions to analyze the properties of images. For example, Feng et al. use normalized cross-correlation to compare two images with a possible rotation or change in scale [25]. Their method involves identifying a relatively small number of points of interest and matching the comparison based on them. The Feng et al. method is insensitive to the rotation of the whole image (i.e. rotation plus translation), while the COOP method is insensitive to the rotation of all vectors without translation. The normalized cross-correlation is a powerful tool, but not appropriate whole cell architectural metric, the COOP is therefore useful for comparing consistency in similarly shaped cells with matching ECM islands, but cannot be used to identify the same cell that has been re-scaled and rotated. Another example of mathematical tools for image analysis is a set of a non-parametric circular statistics tests such as Watson's U_n^2 test, which is designed to evaluate the probability that a sample comes from a specific distribution or that two samples come from the same distribution. For instance, non-parametric circular statistics has been utilized

to evaluate if a pattern of migration of different objects is the same [78, 59]. However, these tests do not consider the location of each sample pair, thus while the results can correspond to the COOP in very special situations these parameters address fundamentally different questions. Thus, these circular statistics tests are not a good tool to evaluate orientational correlation of co-localized pseudo-vectors.

There are specific cases where the COOP will correspond to other parameters. For example, the OOP has been used to quantify the organization of the bacterial population in a channel with respect to the channel direction [75]. Indeed, this is equivalent to a rudimentary case of the COOP where one of the constructs, the channel, is perfectly organized (Fig. 2.3C(ii)-(iii)). The COOP is more general in that it can be used when neither construct is perfectly organized. Circular statistics tool-sets include some correlation metrics [35], such as the circular correlation coefficient [7] which corresponds to the COOP in the same case. Specificically the circular correlation coefficient can only be used for uniform distributions (i.e. isotropic tissues). In that special case, the circular correlation coefficient and the COOP converge to the same equation (A.5). However, the more general vector formulation of the circular correlation coefficient, while not constrained to a uniform distribution, is very complex, and thus cannot be easily characterized the way we have done for the COOP. This circular correlation coefficient would not be a convenient metric for cytoskeleton or cellular orientation quantification. The COOP can be calculated so long as two sets of angular distributions and their locations are known, and it has been extensively characterized. Thus, this new parameter can be used with a multitude of biological systems.

In a healthy, properly functioning cell or tissue, the cytoskeleton needs to be organized in an intricate manner. In disease, loss of this organization leads to reduction in function, such as the myofibril organization changes in dilated cardiomyopathy [37, 76, 4]. However, proper organization of one element in a cell or tissue is not sufficient. The multiple constructs

have to be properly organized with respect to each other, and that organization can have biological implications. This has been shown to occur during maturation of myocytes where the α-actinin is initially punctate and parallel to actin fibrils, but, in mature cardiomyocytes, becomes part of the newly formed sarcomeric Z-lines, which are perpendicular to actin fibrils [60]. In this case the relative orientation of α-actinin staining and actin fibrils indicates the progressive maturation of myofibrils. An additional example where orientation of different constructs affects each other is when the organization of the extracellular matrix can be used to control the architecture of cells [32, 24, 69]. Conversely, cells have been shown to change the orientation of the extracellular matrix fibrils [33]. Another instance of organization correlation can be found in the different cell types and collagen fibrils within heart valves [1]. The common use of such metrics as the OOP and COOP for biological and medical sciences will allow for a quantitative evaluation of tissue engineered substrates from a variety of cell sources. Combining such metrics with histology will create a universal evaluation metric between *in vitro* and *in vivo* systems favorably impacting our ability to design replacement tissues, to create *in vitro* drug testing platforms, and to evaluate pathological reports in the clinic.

Chapter 3

Multi-Scale Characterization of Cardiomyocyte Architecture *in vitro*

[2]

3.1 Introduction

The mechanical pumping of the heart is indisputably a function of the multi-scale architecture of the myocardium [36, 37, 73]. In cardiac tissue engineering, recapitulating this architecture over multiple length-scales has been one of the barriers to the utilization of stem-cell derived cardiomyocytes for fixing the heart and to the creation of *in vitro* platforms for testing cardiotoxicity of pharmaceuticals [62, 26]. For both of these applications, it is increasingly evident that the architecture of the scaffold affects maturity of cells, gene expression levels, and various functional outputs [16, 12, 11, 50, 24, 64, 63]. One affected function is the cells ability to self-assemble into a tissue with optimized

[2] Drew et al., accepted 2016 J Biomech Eng

contractile properties. Learning to leverage the cells' self-assembly capability would allow for tissues to be engineered with minimal input. However, to accomplish this it is necessary to quantify the tissue architecture over many scales and identify the essential cues that promote recapitulation of native tissue structure in engineered cardiac tissue.

During normal development, the heart macro-structure evolves from a tube into a consistent anatomy composed of four chambers wrapped with helical fibers [12, 11, 50, 48, 27, 49, 65]. Similarly, normal primary single cardiomyocytes interrogated for a response to geometrical extracellular matrix (ECM) cues will produce qualitatively consistent structures [32, 61]. However, it is unclear if this consistency holds over all length-scales, and no one has been able to reliably quantify this. Previously, quantifying orientation of architecture in cells has been done using various computational algorithms [10, 43, 23, 77, 51, 44, 79, 52]. Also, prior studies used a variety of metrics to analyze their results that were based on different statistical distributions such as Gaussian [24, 43, 23, 44, 52, 17]. Yet, organizations of structures in cardiac cells are not often normally distributed and one of the best suited parameters for this task is the orientational order parameter. While initially developed for the field of liquid crystals, this parameter has been extensively used to quantify organization in biology [34, 66, 72, 6, 31]. Still, there is no standard method to measure architecture consistency of various structures (actin fibrils, sarcomeric z-lines) over multiple scales to ensure that *in vitro* cells and tissues recapitulate the condition of interest. Quantifying this architecture would also allow us to answer important questions about cells' self-assembly mechanisms. To properly build *in vitro* replicas, it is also essential to quantify the consistency of different subcellular structures organization. This is evident from observing the orientation of α-actinin structures (protein in the z-lines of the myofibril) and the actin fibrils. In development, these two evolve from parallel, punctate, in stress fibers to perpendicular z-lines in myofibrils [22]. In sum, to control the mechanics of engineered heart tissues, it is essential to understand multi-scale consistency of architecture of various structures in cardiac muscle.

The heart architecture has been extensively studied for decades [36, 24, 65, 31, 70, 45, 20]. However, the complex nature of the structures that form the heart makes it challenging to quantitatively describe architecture in a consistent manner. This consistency is essential as the field begins to rely more on cardiac cells and tissues engineered from stem cells [26, 41]. Currently, one popular choice is using induced pluripotent stem cell (iPS) derived cardiomyocytes. However, it has been shown that iPS derived cardiomyocytes do not have all of the functional and structural properties of primary cardiomyocytes [42, 61]. In order to determine why iPS derived cardiomyocytes are different it is necessary to fully understand the cytoskeletal architecture in cardiomyocytes. Yet, the mechanisms behind self-assembly and self-reorganization of cytoskeletal elements within cardiomyocytes remain unknown. To address this uncertainty, we demonstrate how the co-orientational order parameter [20] can be used to elucidate cardiac cell architecture over multiple scales. The qualitative observation of consistent self-assembly as a function of cellular shape was tested over multiple subcellular length-scales, and was found to have implications on these cells contractile function. In addition, we hypothesized that there exists a spatial scale at which there is a distinct change in the consistency of self-assembly and that this spatial scale is constant for cells cultured on ECM islands of any size then the mechanism behind self-assembly is a bottom-up assembly (focal adhesion $\rightarrow$ actin architecture $\rightarrow$ force distributions). In all, this work illustrates the challenge of recapitulating the non-simplistic multi-scale architecture of cardiac cells, but also its importance in creating engineered tissues with proper mechanical function.

3.2 Materials and Methods

Standard methods were used to prepare cells and tissues for structure characterization [32, 20]. Here, we describe them briefly.

3.2.1 Substrate Preparation

Glass coverslips (Fisher Scientific Company, Hanover Park, IL) were sonicated in a 95% ethanol solution for 30 minutes. These coverslips were then spin-coated in polydimethylsiloxane mixed at a 10:1 ratio with curing agent (PDMS, Ellsworth Adhesives, Germantown, WI). The coverslips with PDMS coating were cured at 65℃ overnight.

3.2.2 Extracellular Matrix Printing

Stamp designs were drawn using Adobe Illustrator software (Adobe Systems Inc., San Jose, CA). The designs were etched into 5x5 chrome with soda-lime glass masks by a third-party vendor (FrontRange Photo Mask Co., Palmer Lake, CO). Silicon wafers were made through SU-8 deposition using the glass masks in the Bio-Organic Nanofabrication Facility (University of California, Irvine). In order to create the stamps, silicon wafers were covered in 60-80g of PDMS. It was then cured at 65℃ overnight and peeled from the wafers. Thereafter, the square patterns regions were cut out and stored for use as stamps. The stamps were sonicated and incubated for 1 hour with 0.1 mg/mL drops of fibronectin (Fisher Scientific Company, Hanover Park, IL) placed on top of the patterned faces. Prior to applying fibronectin to the coverslips, the coverslips were UVO-treated. Then the coverslips were incubated in 1% pluronic acid solution (5g Pluronics F-127, Sigma Aldrich, Inc., Saint Louis, MO, dissolved in 500 mL sterile water) for 10 minutes in order to block cell adhesion between regions of fibronectin. After these steps, coverslips were rinsed in Phosphate Buffered Saline (PBS) (Life Technologies, Carlsbad, CA) three times and kept in PBS until cell seeding.

3.2.3 NRVM Harvest and Seeding

All animal protocols were reviewed and approved by the University of California, Irvine, Institutional Animal Care and Use Committee (Protocol No. 2013-3093). Neonatal Sprague-Dawley rats (Charles River Laboratories, Wilmington, MA), 1-3 days postpartum, were sprayed with 95% ethanol and decapitated. The hearts were rapidly removed and trimmed in Hanks Balanced Salt Solution (HBSS) (Life Technologies, Carlsbad, CA). Once all hearts (10 per harvest) were dissected, they were incubated at 4C overnight (12 hours) in a 1 mg/mL trypsin solution (Sigma-Aldrich, Inc., Saint Louis, MO) dissolved in HBSS. The trypsin solution was then removed and tissue was neutralized in warmed M199 culture medium (Invitrogen, Carlsbad, CA) supplemented with 10% heat inactivated Fetal Bovine Serum, 10mM HEPES, 20 mM glucose, 2 mM L-glutamine (Life Technologies, Carlsbad, CA), 1.5 µM vitamin B-12 and 50 U/ml penicillin (Sigma-Aldrich Inc., Saint Louis, MO). The media was removed and the tissue was dissociated through several washes of 1 mg/mL collagenase dissolved in HBSS. The collagenase cell solutions were then centrifuged at 1200 rpm for 10 minutes. The supernatant was aspirated and cells were re-suspended in chilled HBSS. The HBSS cell solution was centrifuged at 1200 rpm for 10 minutes. The supernatant was aspirated and cells were re-suspended in warm 10% FBS M199. The cells were purified in three pre-plate steps, including 45-minute incubations in two different cell culture flasks and a 40-minute incubation in a third cell culture flask (BD Biosciences, San Diego, CA) within a tissue culture incubator. Cells were counted using a disposable hemocytometer (Fisher Scientific, Waltham, MA) and seeded at a density of $1.5x10^5$ or $2.5x10^5$ cells per 3 mL for single cell shape coverslips.

The samples for every experiment were cultured in standard incubator conditions. The dead cells were washed off the samples 24 hours after seeding when media was refreshed with 10% FBS M199 media. The media was replaced by 2% FBS M-199 media 48 hours after seeding to maintain the cardiac myocytes without rapidly increasing the fibroblast population.

3.2.4 Fixing and Staining

After 72 hours in culture, the samples were fixed in 4% paraformaldehyde (PFA) (Fisher Scientific Company, Hanover Park, IL) supplemented with 0.001% Triton X-100 (Sigma Aldrich, Inc., Saint Louis, MO). The samples were each stained for a combination of the following: actin (Alexa Fluor 488 Phalloidin, Life Technologies, Carlsbad, CA), sarcomeric α-actinin (Mouse Monoclonal Anti-α-actinin, Sigma Aldrich, Inc., Saint Louis, MO), nuclei (4,6-diaminodino-2-phenylinodole (DAPI), Life Technologies, Carlsbad, CA), fibronectin (polyclonal rabbit anti-human fibronectin, Sigma Aldrich, Inc., Saint Louis, MO). Secondary staining was done using the appropriate pairs including: tetramethylrhodamine-conjugated goat anti-mouse IgG antibody (Alexa Fluor 633 Goat Anti-Mouse, Life Technologies, Carlsbad, CA), and goat anti-rabbit IgG antibodies (Alexa Fluor 750 goat anti-rabbit, Life Technologies, Carlsbad, CA). Coverslips with stained cells were mounted onto glass cover slides (VWR, Radnor, PA) with ProLong Gold Antifade Reagent (Life Technologies, Carlsbad, CA) to prevent stain bleaching. Nail polish (Electron Microscopy Sciences, Hatfield, PA) was then used as sealant along the edge of each coverslip. The sealant was allowed to dry overnight.

3.2.5 Imaging

Cover slides with immunostained samples were imaged on an IX-83 inverted motorized microscope (Olympus America, Center Valley, PA) mounted with a digital CCD camera ORCA-R2 C10600-10B (Hamamatsu Photonics, Shizuoka Prefecture, Japan) using an UPLFLN 40x oil immersion objective (Olympus America, Center Valley, PA).

3.2.6 Image Analysis: Single Cells

Image analysis of single cells was performed using previously created customized MATLAB codes. These codes were used to determine construct orientation and calculate the COOP [20]. Grid squares were placed over the entire image and the director, i.e. average orientation, was calculated in each grid square. The area of the cells was approximately 1250 μm^2 and 2500 μm^2, which is equivalent to a length-scale of 35 µm and 50 µm respectively. Therefore, the possible sizes of the grid squares used to analyze single cardiomyocytes could range from 1 µm to 35 µm or 1 µm to 50 µm. We chose the large length scale (21 µm) for cells with area $\sim$1250 μm^2 by determining the largest scale that contained a minimum of two orientation angles within two grid squares for all cell shapes. The large length scale (29 µm) for cells with area $\sim$2500 μm^2 was determine using the same method used to select cells with area $\sim$1250 μm^2 large length scale. Pairwise comparisons were used to quantify the consistency of cardiomyocytes of same shape and aspect ratio.

3.2.7 Statistics

To determine statistical significance, one-way ANOVA was used with the Holm-Sidak post-hoc test, which is commonly used for pairwise comparison of experimental groups. Significance was considered for an unadjusted p-value less than the critical level, which accounts for the number of comparisons.

3.2.8 EC50 and AUC

To determine spatial scales where a distinct change in consistency could be seen for the differently shaped cardiomyocytes, the EC50 was calculated from fitting the average COOP values at multiple length scales from 1 µm to 35 µm or 1 µm to 50 µm with a four parameter

logistic curve. Also, the normalized COOP was calculated at every length scale based on (Eq. 3.1):

$$normalized\ COOP = \frac{x-a}{b-a} \tag{3.1}$$

where x is the original COOP value, a is the COOP at that length scale 1 µm and b is the the COOP at either 21 µm or 29 µm. Then to the fit the normalized COOP data at multiple length scales the four parameter logistic curve was used and the area under the parametric curve (AUC) was calculated. The AUC was also used to explore and determine if there was spatial scales of distinct change in consistency for all of the differently shaped cells.

3.3 Results

Characterizing cardiac muscle architecture is inherently a multi-scale problem. To address this, the consistency of self-assembly of single cardiomyocytes over multiple length-scales was considered. There are three questions of interest when considering single cells: (1) how does consistency of self-assembly change in a multi-scale way, (2) how does extracellular matrix (ECM) cues affect consistency of self-assembly and (3) how does size of ECM affect consistency of self-assembly? In cell shapes with parallel fibers (i.e. rectangles with high aspect ratio) it is possible to evaluate consistency based on the variance of a simple order parameter. For cells that have un-aligned myofibrils (i.e. squares) the orientational order parameter (OOP) would be always low, and the variance would be independent of consistency. To overcome this, the co-orientational order parameter (COOP) was utilized to evaluate consistency of self-assembly in cells of various shapes, aspect ratios, and sizes. This provided a method to evaluate consistency as a function of scale in single cardiomyocytes by culturing neonatoal rat ventricular myocytes (NRVMs) on fibronectin islands of rectangles, ovals, and triangles of various aspect ratios and sizes (Table 3.1 and

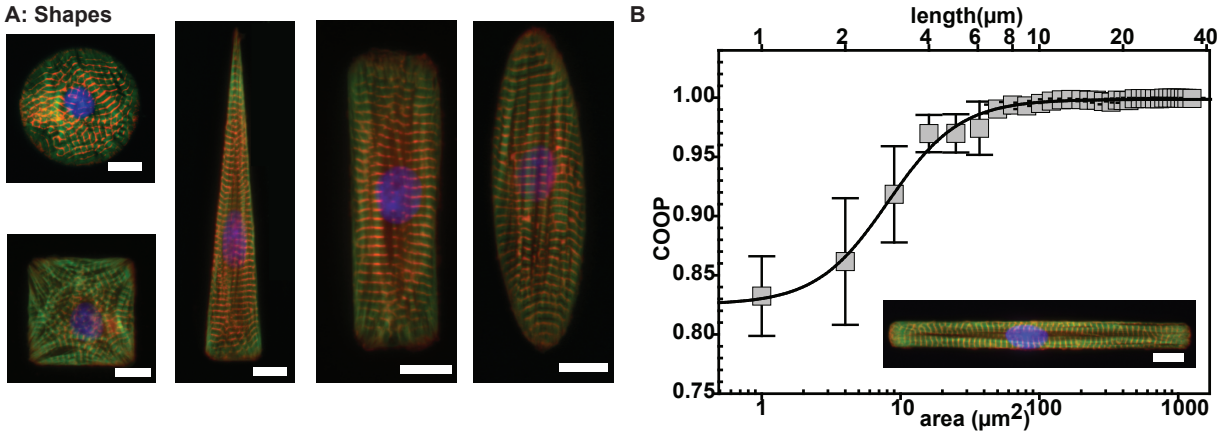

Figure 3.1: **Example of Actin fibril consistency in NRVM with area $\sim$1250μm^2.**(A) Images of stained NRVMS cultured on various shaped FN islands. The stains in the images are green for actin, red for *alpha*-actinin, and blue for nuclei. (B) The average COOP for consistency of actin fibril organization at different area and length-scales in rectangular shaped NRVMs with an aspect ratio$\sim$11. Scale bars=10 µm.

Fig. 3.1A).

3.3.1 Cells with Area $\sim$1250 μm^2

The COOP was calculated to quantify consistency of actin fibrils and sarcomeric z-lines for a variety of subcellular length-scales (Fig. 3.1B). For all shapes, the COOP varied from low values at small length-scales to high values at large length-scales (Fig. 3.2). To summarize, the consistency data of actin fibrils and sarcomeric z-lines in cells with area $\sim$1250 μm^2 was plotted for all shapes at a small length-scale of $\sim$1 µm (Fig. 3.2A and Fig. 3.3A) and at a large length-scale of $\sim$21 µm (Fig. 3.2B and Fig. 3.3B). Consistency of self-assembly at the small scale ($\sim$1 µm) was highly dependent on the aspect ratio of the ECM island (Fig. 3.2A and Fig. 3.3A). Furthermore, consistency of actin fibrils was significantly different between circles (ovals with aspect ratio of 1) and various shapes with an aspect ratio of $\sim$1 (Fig. 3.2A). This difference in circular shaped cardiomyocytes could be due to the rotational symmetry of the shape. Actin fibril consistency in triangular cells with an aspect ratio of 1.95 were significantly different than oval shaped cells with aspect ratios of 1.70 and 2.45

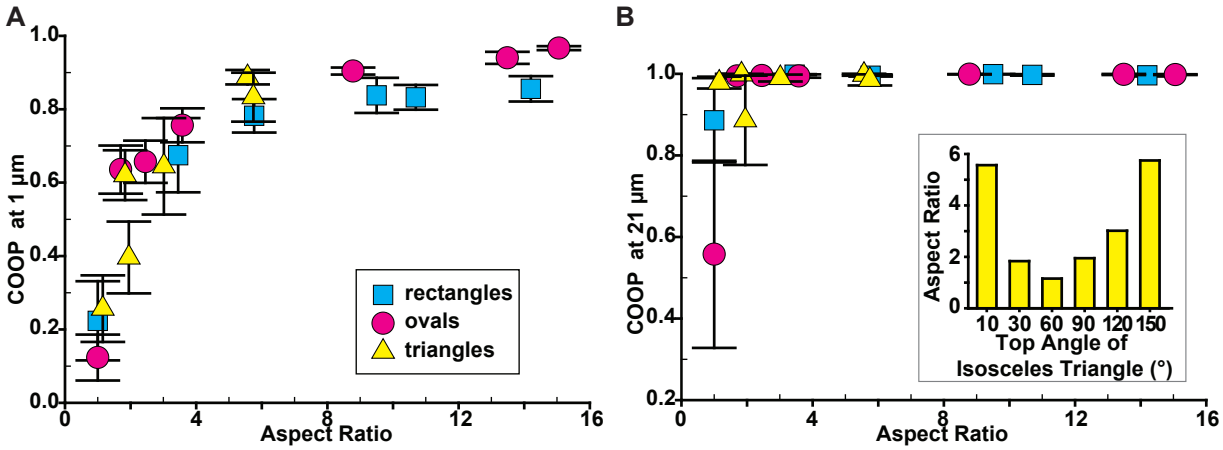

Figure 3.2: **Actin fibril consistency for various aspect ratios in cells with area ∼1250 μm^2.** The average COOP for consistency of actin fibril organization for different aspect ratios at the small length-scale of 1 µm (A) and at the large length-scale 21 µm (B). Inset of (B) shows aspect ratios for the isosceles triangle shapes.

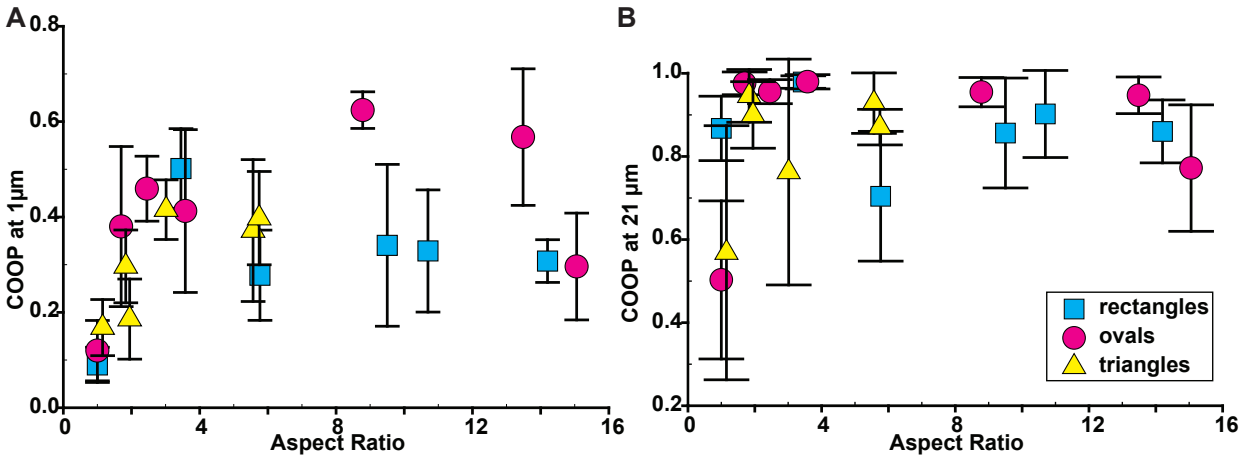

Figure 3.3: **Sarcomeric z-line consistency for various aspect ratios n cells with area ∼1250 μm^2.** (A) The average COOP for consistency of sarcomeric z-lines organization for different aspect ratios at the small length-scale (1 µm). (B) At the large length-scale (10 µm) the average COOPs for consistency of sarcomeric z-lines organization for different aspect ratios.

(Fig. 3.2A). Also, the consistency of actin fibrils in triangular cells with an aspect ratio of 3.02 were significantly different than oval shaped cells with an aspect ratio of 3.58 (Fig. 3.2A). Additionally, actin fibril consistency in oval shaped cardiomyocytes with aspect ratios of 13.49 and 15.06 were significantly different than rectangular cardiomyocytes with an aspect ratio of 14.20 (Fig. 3.2A). In fact, at this small scale, the consistency of actin fibrils settles at an aspect ratio of ∼6, which correlates with the known relationship between force and aspect ratio [47]. The average COOP at a scale of 1 µm for shapes with aspect ratios $AR > 5.5$ was 0.87 and 0.39 for actin (Fig. 3.2A) and sarcomeric z-lines (Fig. 3.3A), respectively. Except for the circle, the shaped NRVMs were consistent at length-scales of ∼21 µm (area=441μm^2) and above, with an average COOP of 0.98 and 0.87 for actin (Fig. 3.2B) and sarcomeric z-lines (Fig. 3.3B), respectively. The oval with an aspect ratio of one, i.e. a circle, was shown to be less consistent than other shapes at large scales (Fig. 3.2B and Fig. 3.3B) because it has the added challenge of shape rotational symmetry, but it has also been inconsistent qualitatively [32]. For all other shapes, the qualitative observation of consistent cell self-assembly of actin fibrils was confirmed by this data for large length-scales. This data illustrated that it is possible to elucidate the self-assembly consistency in single cells, but architecture in larger single cells needed to be characterized as well.

3.3.2 Cells with Area ∼2500 μm^2

In fact, we explored actin fibril and sarcomeric z-line consistency in cardiomyocytes with bigger areas (∼2500 μm^2). The average COOP for actin fibirls and sarcomeric z-lines was calculated at the small length scale of ∼1 µm for these bigger cardiomyocytes of various shapes (e.g. rectangles, ovals, and triangles) (Fig. 3.4A-F). Similar to cells with smaller areas, the consistency of self-assembly for cells with larger areas was highly dependent on aspect ratio at this small scale. Furthermore, at ∼1 µm there was significant difference between actin fibril consistency for rectangles and ovals with aspect ratios of 1.00 (Fig. 3.4A,C). Also,

Table 3.1: **The single cell shapes.** Shape types, their aspect ratios, and the sample size for each.

Type of Shape	Aspect Ratio	Sample # Area 1250	**Sample # Area 2500**
rectangle	1.00	6	**8**
rectangle	**3.26**	0	**4**
rectangle	3.45	5	0
rectangle	5.77	4	0
rectangle	**5.91**	0	**4**
rectangle	9.50	6	0
rectangle	10.69	5	0
rectangle	**13.20**	0	**3**
rectangle	14.20	5	0
oval	1.00	6	**5**
oval	1.75	5	0
oval	**2.10**	0	**5**
oval	2.45	6	0
oval	**3.47**	0	**6**
oval	3.58	6	0
oval	**8.59**	0	**3**
oval	8.78	4	0
oval	13.49	8	0
oval	15.06	5	0
triangle 60°	1.15	5	**4**
triangle 30°	1.83	7	0
triangle 30°	**1.93**	0	**6**
triangle 90°	1.95	7	0
triangle 90°	**3.05**	0	**5**
triangle 120°	**2.96**	0	**4**
triangle 120°	3.02	4	0
triangle 10°	5.57	4	0
triangle 10°	**6.10**	0	**4**
triangle 150°	**5.46**	0	**4**
triangle 150°	5.75	5	0

triangles with aspect ratio 3.05 actin fibril consistency was significantly different from other shapes with similar aspect ratios and areas of ∼2500 μm^2 (Fig. 3.4A,C,E). Actin fibril and sarcomeric z-line consistency was also calculated at ∼21 µm as well (Fig. 3.5A-F). At ∼21 µm, there was no significant difference between actin fibril or sarcomeric z-line consistency of various shapes with similar aspect ratios and areas of ∼2500 μm^2 (Fig. 3.5A-F).

Since these cardiomyocytes are twice the size of the smaller cells we also explored actin fibril and sarcomeric z-line consistency at a larger length scale (∼29 µm) (Fig. 3.6). At this large scale of ∼29 µm there was significant difference between actin fibril consistency of rectangles with an aspect of 1.00 and triangles with an aspect ratio of 1.15 (Fig. 3.6A). Also, ovals with an aspect ratio of 3.47 were significantly difference from triangles with an aspect ratio of 3.05 (Fig. 3.6A). However, at ∼29 µm there was no significant difference between sarcomeric z-line consistency of various shapes of similar aspect ratios and areas (Fig. 3.6B).

3.3.3 Comparing Cells with Different Areas

In addition, we compared the consistency of actin fibrils and sarcomeric z-lines in similar shapes with different areas (Fig. 3.4 and Fig. 3.5). At the small scale (∼1 µm), there was no significant difference between shapes of similar aspect ratios with different areas for actin fibril consistency (Fig. 3.4A,C,E). However, for sarcomeric z-line consistency there was significant difference between ovals with similar $AR > 1.00$ with different areas (Fig. 3.4D). Also, sarcomeric z-line consistency for triangles of different areas with a top angle of 120 and 150 degrees were significantly different at ∼1 µm (Fig. 3.4F). Additionally at this scale there was a significant difference between rectangles of different areas with aspect ratios of ∼3 for sarcomeric z-lines (Fig. 3.4B). In sum, sarcomeric z-line consistency was effected by ECM island size for ∼44% (7/16) of the shapes. Similarly, we compared the consistency of actin fibrils and sarcomeric z-lines at the length scale of ∼21 µm for similar shapes with different

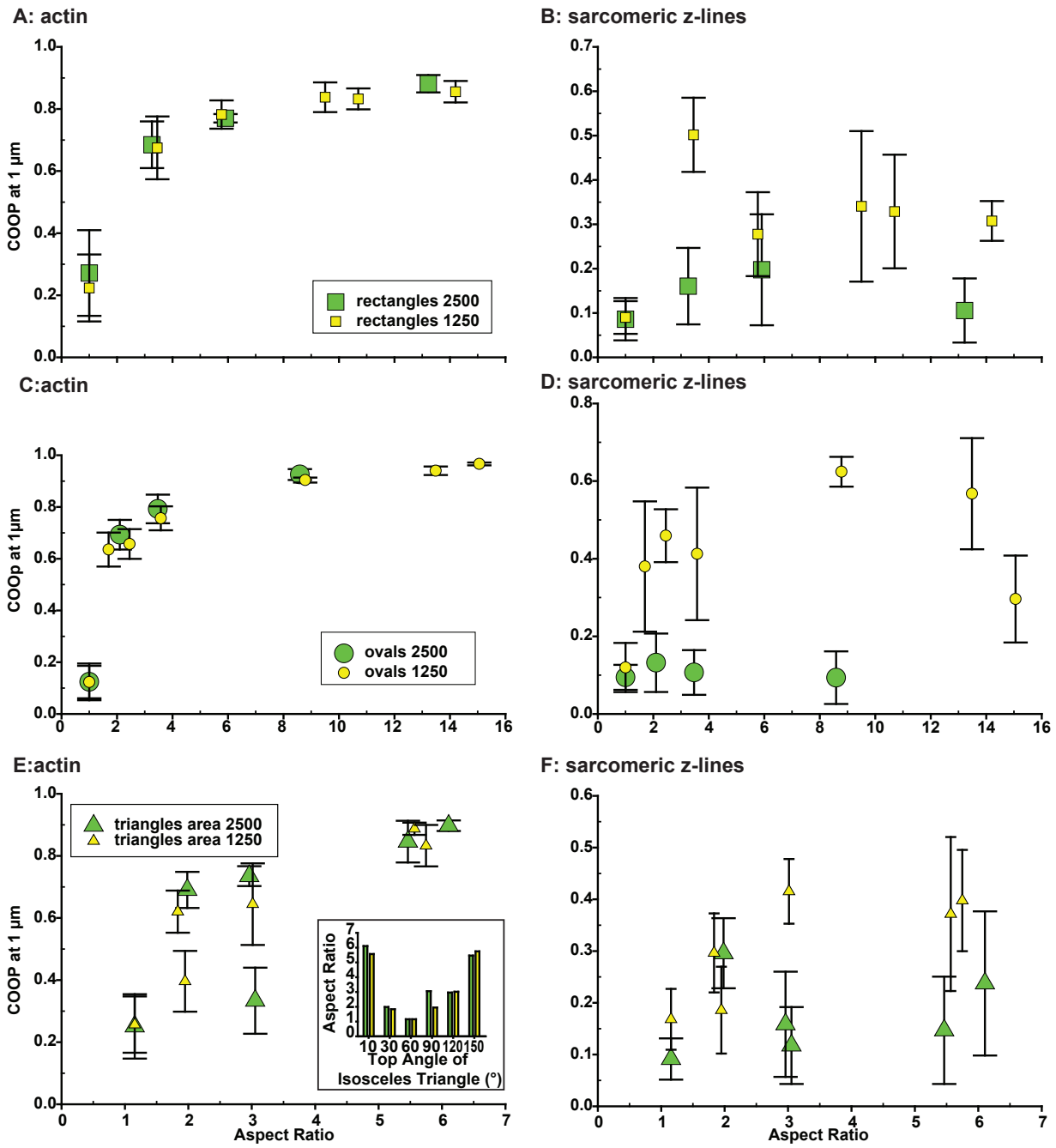

Figure 3.4: **Consistency for differently shaped cardiomyocytes with a variety of aspect ratios and areas at 1 µm.** (A) The average COOP for consistency of actin organization for rectangular cells. (B) The average COOP for consistency of sarcomeric z-lines organization for rectangular cells. (C) The average COOP for consistency of actin organization for cells shaped into ovals. (D) The average COOP for consistency of sarcomeric z-lines organization for cells shaped into ovals. (E) The average COOP for consistency of actin organization for triangular cells. (F) The average COOP for consistency of sarcomeric z-lines organization for triangular cells. inset of (E) shows aspect ratios for the isosceles triangle shapes. Green colored cells have an area of $\sim$2500 μm^2 and yellow colored cells have an area of $\sim$1250 μm^2.

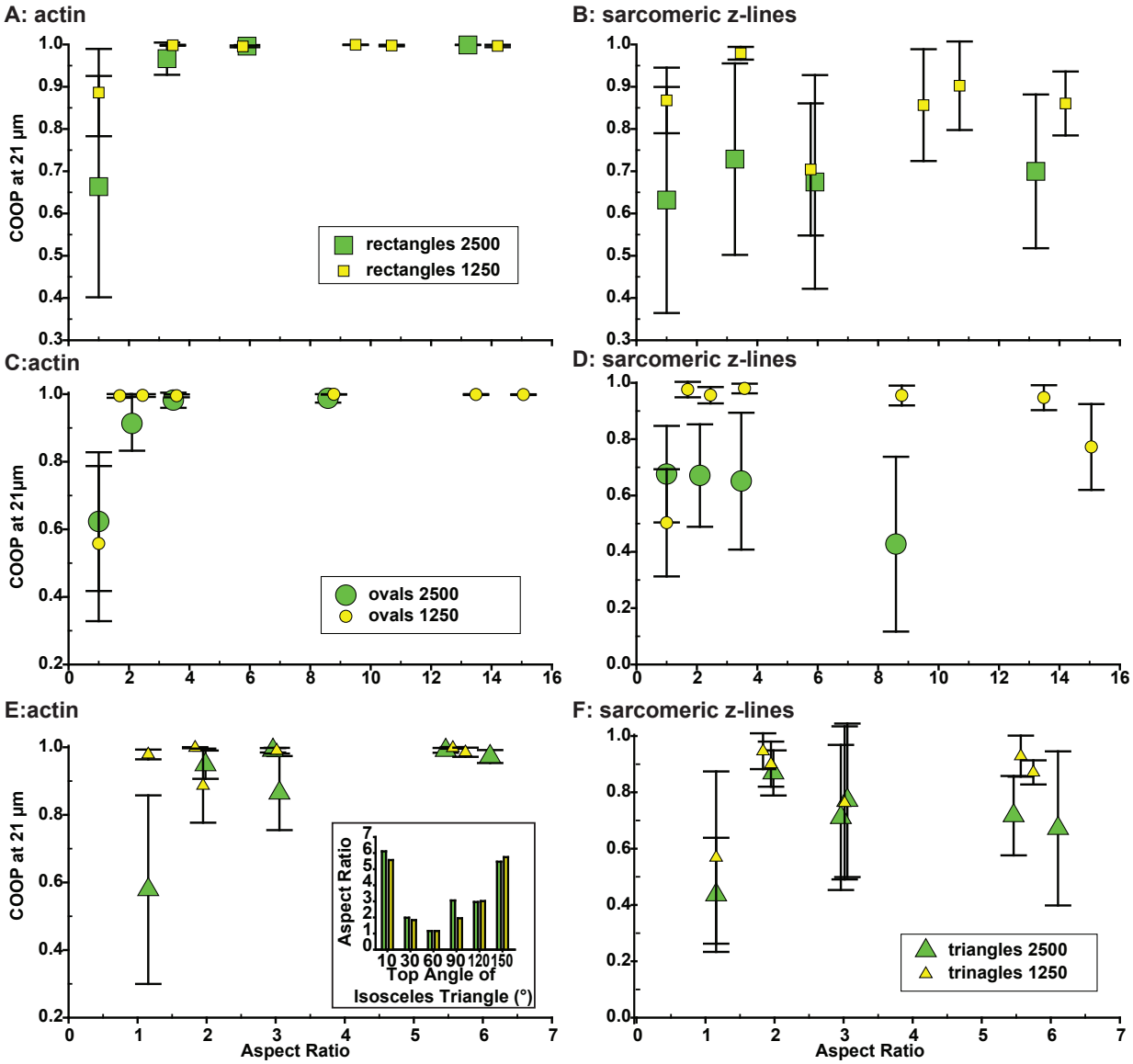

Figure 3.5: **Consistency for differently shaped cardiomyocytes with a variety of aspect ratios and areas at 21 µm.** (A) The average COOP for consistency of actin organization for rectangular cells. (B) The average COOP for consistency of sarcomeric z-lines organization for rectangular cells. (C) The average COOP for consistency of actin organization for cells shaped into ovals. (D) The average COOP for consistency of sarcomeric z-lines organization for cells shaped into ovals. (E) The average COOP for consistency of actin organization for triangular cells. (F) The average COOP for consistency of sarcomeric z-lines organization for triangular cells. inset of (E) shows aspect ratios for the isosceles triangle shapes. Green colored cells have an area of $\sim$2500 μm^2 and yellow colored cells have an area of $\sim$1250 μm^2.

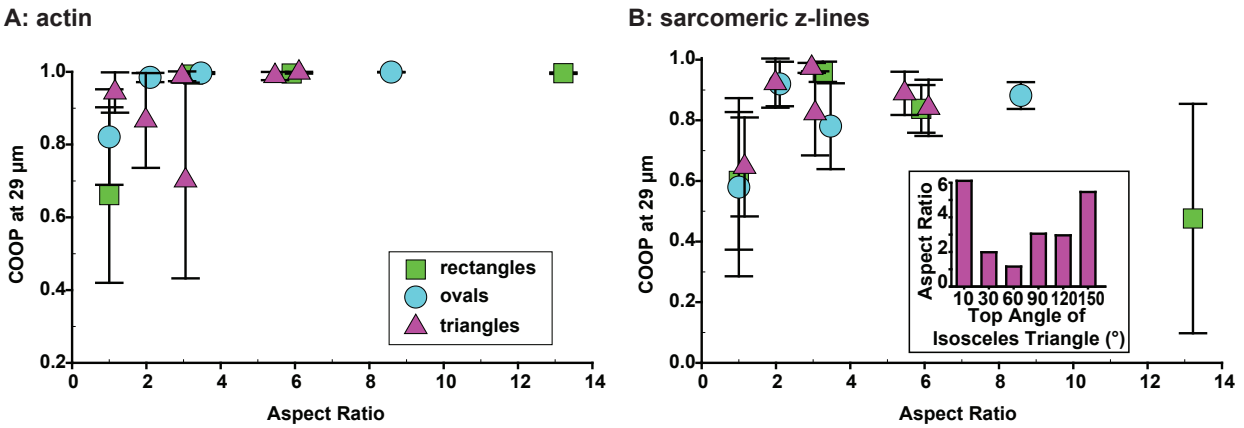

Figure 3.6: **Actin and Sarcomeric z-line consistency for various aspect ratios in cells with area ∼2500 μm^2 at 29 µm.** The average COOP for consistency of actin fibril (A) and sarcomeric z-lines (B) organization for different aspect ratios at the large length-scale of 29 µm.

areas (Fig. 3.5A-F). At ∼21 µm, there was only a significant different between rectangles of different areas with an aspect ratio of 1.00 for actin fibrils consistency (Fig. 3.5A). Also, there was a significant different between rectangles of different areas with an aspect ratio of 1.00 for sarcomeric z-line consistency at ∼21 µm (Fig. 3.5B). As well as a significant different for sarcomeric z-line consistency between ovals of different areas with similar aspect ratios greater than one (Fig. 3.5D). Overall, at the length scale of ∼21 µm, ECM island size only had an effect on acitn fibril consistency for ∼0.06% (1/16) of the shapes. Whereas, sarcomeric z-line consistency was shown to be effected by ECM island size for ∼31% (5/16) of the shapes.

3.3.4 Spatial Scale of Distinct Change in Actin Consistency

In order to determine if there was a spatial scale of distinct change in actin fibril consistency we calculated the EC50 for the various shapes with different areas (Fig. 3.7A,B,C). EC50 values for rectangular and oval shaped cells appeared to be linear with aspect ratio (Fig. 3.7A,B). However, EC50 values did not appear to be linear with

aspect ratio for triangular shaped cardiomyocytes (Fig. 3.7C). Furthermore, the EC50 value was extremely high and unrealistic for larger triangles with an aspect ratio of 1.15 (Fig. 3.7C). Therefore, we were not able to determine if there was a distinct change in actin fibril consistency from the EC50 values. Thus, we calculated the area under the curve (AUC) for the various shapes with area of $\sim$1250 μm^2 (Fig. 3.8A) and an area of $\sim$2500 μm^2 (Fig. 3.8A) to determine if there was a distinct change in actin fibril consistency. The AUC ranged from 14 to 19 for rectangular and oval shaped cells with an area of $\sim$1250 μm^2 (Fig. 3.8A). Whereas, rectangular and oval shaped cells with an area of $\sim$2500 μm^2 had AUC values that ranged from 16 to 25 (Fig. 3.8B). Triangular shaped cells with an area of $\sim$1250 μm^2 had AUC values that were more dispersed that ranged from 9 to 16 (Fig. 3.8A). In addition, AUC values were dispersed and ranged from 14 to 28 for the bigger triangular shaped cells with an area of $\sim$2500 μm^2 (Fig. 3.8B). To summarize the AUC results we calculated the average AUC for each shape for both areas (Fig. 3.9). We found there was no significant difference between the average AUC for rectangular and oval shaped cardiomyoycte with different areas (Fig. 3.9). Conversly, the average AUC for triangular shaped cells was significantly difference between cells with area $\sim$1250 μm^2 and $\sim$2500 μm^2 (Fig. 3.9). Overall, our results show that the average AUC was constant for 2 out of 3 (66%) ECM island shapes of different sizes.

3.4 Discussion

In this work we illustrated the use of one order parameter, the co-orientational order parameter [20] in characterizing multi-scale organization of engineered cardiac cells. Indeed, there were other metrics that could have been used to summarize orientation properties from data obtained through image analysis that are based on a variety of functions. For example, there are different statistical metrics based on different

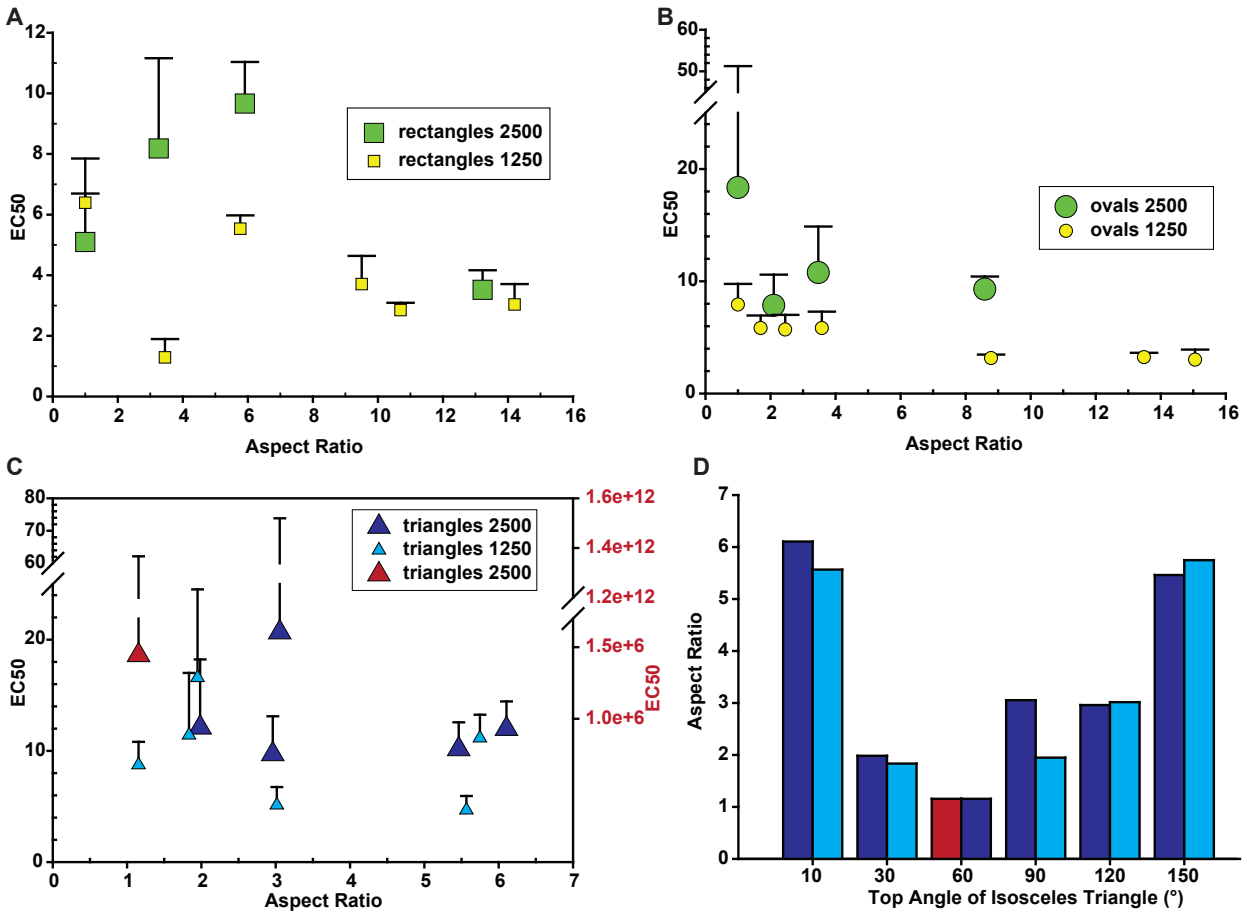

Figure 3.7: **Actin fibril EC50.** The actin fibril EC50 for rectangular (A), oval (B), and triangular (C) cells with areas of ∼1250 μm^2 and ∼2500 μm^2. The red triangle corresponds to the right EC50 axis. (D) shows aspect ratios for the isosceles triangle shapes.

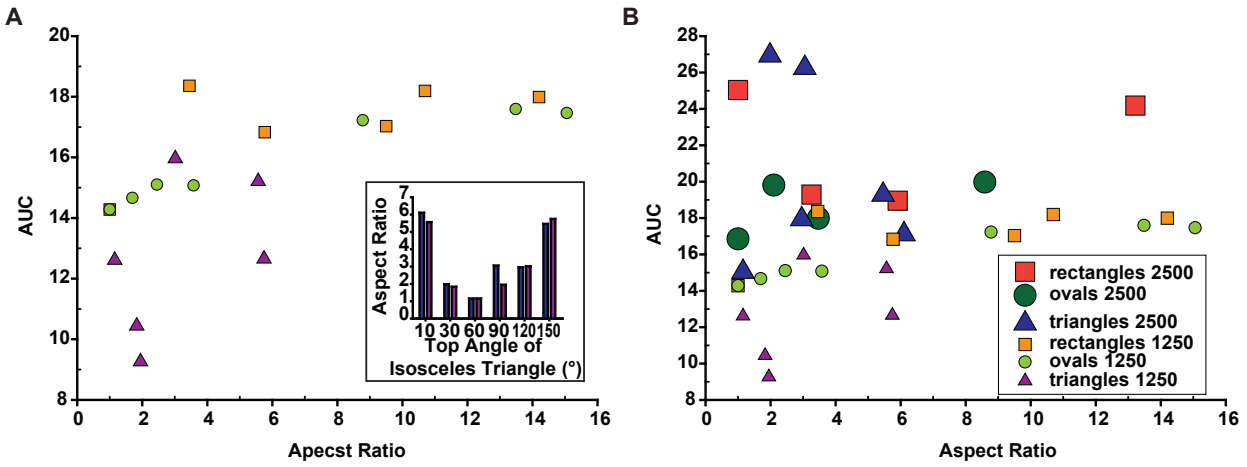

Figure 3.8: **Actin fibril area under the curve.** The actin fibril area under the curve for various shapes and aspect ratios for cells with an area of ∼1250 μm^2(A) and an area of ∼2500 μm^2 (B). Inset of (A) shows aspect ratios for the isosceles triangle shapes.

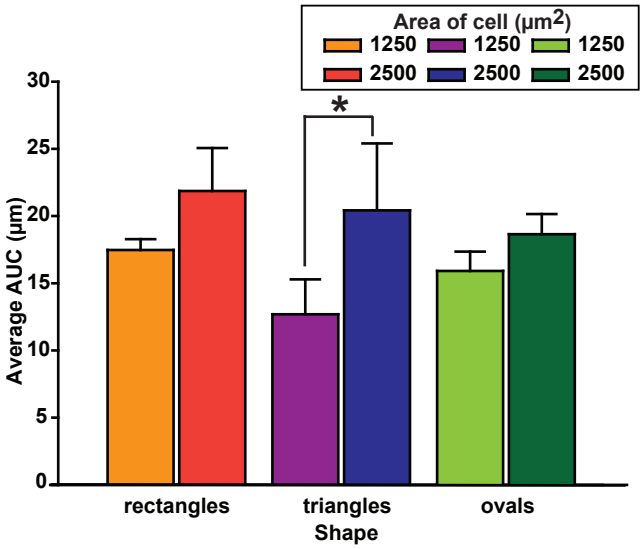

Figure 3.9: **Average area under the curve for actin fibrils.** The average actin fibril area under the curve for rectangles, triangles and ovals with an area of ∼1250 μm^2 and an area of ∼2500 μm^2, (*) indicates statistical significance.

distributions that were used to quantify orientation data [17, 43, 23] or multiple image correlation methods to compare images [15, 25, 54, 35]. However, the COOP was chosen because it is mathematically appropriate to interpret data from biological tissues and, by now, have been widely characterized for the use in cardiac tissues [20]. These methods and software could have also been used on immunostatined images of fibronectin as well [5], however examining ECM was beyond the scope of this paper.

There have been many models of single cell self-assembly, but they have mostly relied on a qualitative view of cytoskeletal architecture for validation [32, 19, 55, 21]. The ability to quantify consistency displayed in this work provides a tool for future models not only to be validated quantitatively, but to be assessed at multiple length-scales (Fig. 3.1B). Indeed, by considering architecture over multiple length-scales, we discovered that the highest actin fibril consistency at smaller subcellular length-scales was observed with high aspect ratios, e.g. elongated cells, without sharp corners of the ECM island. Therefore, at small length-scales in order for actin fibrils to consistently self-assemble it is more advantageous for cells to be a smooth elongated shape. The consistency settled at a very high value for the small

subcellular scale of 1 µm when the aspect ratio is above ∼6 (Fig. 3.2A and Fig. 3.4A,B,C). This has an interesting correlation with the TFM data showing a maximum force produced by cells with an aspect ratio of 6-7 [47]. Thus, in order to produce reliably high forces the cell needs to be assembled consistently within areas that range $1\mu m^2$ ∼400 μm^2 (Fig. 3.2), or conversely, given proper guidance, cardiomyocytes can be assembled very consistently with areas of 3 orders of magnitude in scale. In addition, we observed that actin fibril consistency at both length scales 1 µm and 21 µm, (Fig. 3.4A,C,E and Fig. 3.5A,C,E) were similar between cells of similar shapes and aspect ratios with different areas. Overall, at both of these scales, the consistency of actin fibrils was not signficantly different for ∼99% of shapes with similar aspect ratios with different areas. Thus, we discovered that self-assembly of actin fibrils does not depend on the size of the ECM island (Fig. 3.4A-F and Fig. 3.5A-F).

Furthermore, using the area under the curve we were able to discover distinct spatial scales in the self-assembly of actin fibril consistency for cardiomyocytes on different ECM island sizes. The distinct average spatial scales of actin fibril consistency was constant for rectangular and oval shaped cardiomyocytes with different areas. However, it was surprising that the distinct average spatial scale of actin fibril consistency was not constant for triangular shaped cardiomyoyctes with different areas. There are a few possible explanations for this unexpected results. First, grids of a variety of sizes were used to determine consistency at each length scale tested, but grids might not be an appropriate way to obtain consistency values for multiple length scales for triangular shaped cells. There does not appear to be logical effective way to place grids over triangles. It might be more applicable to define a partition that follows the nature shape of the triangle instead. Second, It would be expected that the triangles would have the same aspect ratio for isosceles triangles with similar angles no matter the ECM island size. However, the aspect ratio of triangular shaped cells with a top angle of 90 degrees increased by 1.10 between ECM islands with areas of ∼1250 μm^2 and ∼2500 μm^2. Nonetheless, 66% of the average distinct spatial scales of actin fibril was constant were cells on ECM islands of different

sizes. As a result, we concluded that distinct spatial scales of self-assembly for actin fibril consistency in cardiomyocytes *in vitro* was constant for cells on a differently sized ECM islands. Therefore, this is further evidence that the mechanism behind self-assembly is based on bottom-up assembly.

In summary, the quantitative analysis of primary engineered cardiac cells illuminated an important property, self-assembly and force development mechanisms are optimized at the same minimal aspect ratio. In addition, we showed that ECM island size does not effect consistency of actin fibrils and sarcomeric z-lines. As well as showing that ECM island size does not effect the distinct spatial scales of self-assembly of actin fibrils. Lastly, providing evidence that the mechanism behind self-assembly is based on assembly from the bottom-up.

Chapter 4

Multi-Scale Quantification of Cardiomyocytes Intracellular Architecture *in silico*

4.1 Introduction

Organs in the body are intricately organized on a wide range of length scales. In the heart, organization is seen at length scales that span several orders of magnitude (from nanometers to centimeters), and organization at one scale can differ from organization at another scale. For instance, z-lines and actin filaments, which are the major building blocks of sarcomeres, have particular patterns of organization at the nanometer length scale, whereas myofibrils, which are made up of many sarcomeres, can show an independent organization at the centimeter length scale. The collective organization at all of these length scales greatly affects the emergent pumping function of cardiomyocytes and the heart as a whole, and in diseased hearts, organization is known to be disturbed on some

length scales. However, the mechanisms of self-assembly or self-reorganization, which could be paramount in heart disease, are not fully understood.

Currently, it is known that assembly of this multi-scale architecture is controlled by myofibrillogenesis (formation of myofibrils) processes. Also, boundary conditions, migration, and mechanotransduction influence the self-assembly of the intracellular structures. For instance, cell shape is controlled by extracellular matrix (ECM) boundary conditions. Previously, it has been shown that the cell shape affects the organization of myofibrils [9]. *In vitro* data has shown that cells engineered with corners e.g. squares, triangles contain myofibrils that span the longest diagonal of the cells and with focal adhesion located in the corners of the cells [9, 32]. Yet, shapes with smooth curves e.g. circles have a random organization of myofibrils and focal adhesions scattered randomly along the boundaries of the cell [32].

Several computational models have been proposed to mimic myofibrillogenesis and predict the organization of myofibrils and focal adhesions in cells. Novak et. al. created a model that is able to recapitulate the distribution of focal adhesion [55]. However, their model was validated with fibroblast instead of cardiomyocytes. Deshpande et. al. used finite elements to create a model of the distribution of myofibrils [18, 19]. They use the interaction between stress fibers, integrins, and the substrate of the cell. This model was able to predict myofibril distribution for a variety of shapes. Yet, their model was not validated with cardiomyocytes but with fibroblast and epithelial cells. Also, Paszek et. al. created a chemo-mechanical model capable of predicting the stresses and strains of focal adhesions [57]. Their model is based on the interaction between integrins and ligands. Unlike the other models, they did not use a specific cell type to validate their model.

Our lab's PI previously created a cardiomyocyte specific myofibrillogenesis model based on concepts from Novak et. al. model and the interaction of integrins and myofibrils [32]. Our model was validated with cardiomyocytes and predicts myofibril and focal adhesion

distribution. This model has been developed in such a way as to be modular. In this chapter, we added length scales to our model and validated the model using the co-orientational order parameter (COOP) to quantitatively compare the consistency of actin orientation in the model to the experimental data collected in Chapter 3. We hypothesized that the model should be accurate for larger length scales, but will be less accurate at smaller length scales. This will considerably extend the use of the model, and it might become possible to include factors such as motility. Creating a more robust myofibrillogenesis model will greatly enhance our ability to understand the mechanisms in cells that do not function like normal cardiomyocytes.

4.2 Methods and Materials

4.2.1 Microcontact printing and ECM islands

To make the substrates, PDMS (Ellsworth Adhesives, Germantown, WI) was spin-coated on glass coverslips (Fisher Scientific Company, Hanover Park, IL). These PDMS coated coverslips were cured in a 60 degrees Celsius oven overnight. Microcontact printing was used to create a variety of shaped myocytes. Adobe Illustrator(Adobe Systems Incorporated, San Jose, CA) was used to design a stamp with various shapes of different areas and aspect ratios. A third party vendor (FrontRange Photo Mask Co., Palmer Lake, CO) created mask from the stamp design. A silicon wafer (Integrated Nanosystems Research Facility, Irvine, CA) was created from the mask. Silicon wafers were coated in PDMS and cured at 60 degrees overnight. The PDMS was peeled from the wafers, and was stored as PDMS stamps. The extracellular matrix (ECM) protein Fibronectin (FN) (Fisher Scientific Company, Hanover Park, IL) was transferred from these stamps onto UV-sterilized (UVO, Jelight Company, Inc. Irvine, CA) PDMS coated coverslips. To block cell adhesion between regions of fibronectin,

substrates were washed with pluronics (250g of Pluronics F-127, Sigma Aldrich, Inc., Saint Louis, MO) for ten minutes. Followed by three rinses of Phosphate Buffered Saline (PBS) (Life Technologies, Carlsbad, CA) and stored at 4 degrees Celsius prior to cell seeding.

4.2.2 NRVM Harvest and Seeding

All experiments were conducted in accordance with the guidelines of the Institutional Animal Care and Use Committee of UCI (protocal No.2013-3093). Ventricular tissue was removed from one to three day old neonatal Sprague Dawley rats (Charles River Laboratories, Wilmington, MA). The tissue was placed in 1 mg/mL trypsin solution (Sigma-Aldrich, Inc., Saint Louis, MO) overnight (12 hour incubation) at 4 degrees Celsius. The next day, the tissue was dissociated into single cells by treating four times with 1 mg/mL collagenase type II (Worthington Biochemical, Lakewood, NJ) for two minutes at 37 degrees Celsius. The cell solution was filtered and remaining cells were purified using three pre-plate steps. After purification, cells were seeded on coverslips at density of $1.5x10^5$ or $2.5x10^5$ cells per 3 mL.

4.2.3 Fixing and Staining

After 3 days in culture, cardiomyocytes were fixed in 4% paraformaldehyde (PFA) (Fisher Scientific Company, Hanover Park, IL) with 0.001% Triton X-100 (Sigma Aldrich, Inc., Saint Louis, MO). Cardiomyocytes were stained with the following combination: sarcomeric α-actinin (Mouse Monoclonal Anti-α-actinin, Sigma Aldrich, Inc., Saint Louis, MO), actin (Alexa Fluor 488 Phalloidin, Life Technologies, Carlsbad, CA), fibronectin (polyclonal rabbit anti-human fibronectin, Sigma Aldrich, Inc., Saint Louis, MO), and nuclei (4,6-diaminodino-2-phenylinodole (DAPI), Life Technologies, Carlsbad, CA). Secondary staining was peformed using tetramethylrhodamine-conjugated goat anti-mouse IgG antibody (Alexa Fluor 633

Goat Anti-Mouse Life Technologies, Carlsbad, CA) and goat anti-rabbit IgG antibodies (Alexa Fluor 750 goat anti-rabbit, Life Technologies, Carlsbad, CA).

4.2.4 Imaging

To collect images of the immunostained single cells an IX-83 inverted motorized microscope (Olympus America, Center Valley, PA) with an UPLFLN 40x oil immersion objective (Olympus America, Center Valley, PA) was used. Also the microscope was mounted with a digital CCD camera ORCA-R2 C10600-10B (Hamamatsu Photonics, Shizuoka Prefecture, Japan).

4.2.5 Image Analysis

Previously customized MATLAB codes were used to analyze images of single cells [20]. These codes calculated construct orientation angles of sarcomeric z-lines and actin fibers in the images [20].

4.2.6 Model

Output from a previously myofibrillogenesis model was used to create *in silico* cardiomyocytes of various shapes, areas, and aspect ratios [32]. The previous model is a phenomenological reaction diffusion model based on interaction between focal adhesions and myofibrils [32] and is specific to cardiomyocytes. Equations for the model can be found in the work done by Grosberg et al. [32]. We added length scale information to we created triangles and rectangles with a variety of aspect ratios and areas similar to experimental data obtained in Chapter 2. Furthermore, we were able to create circles e.g. ovals with an

aspect ratio of one. The parameters used to create cells were similar to the ones used in the study by Grosberg et al. [32].

Incorporating length scales into the model

Originally all shapes had an area of one in the model with arbitrary units. Therefore we created a customized MATLAB codes to add length scales into the model. First, this code was used to add units and to change the area, height, and width of the shapes from the model to match the corresponding *in vitro* shaped cells. Second, interpolation was used to fill in the corresponding actin orientation angles for every pixel inside of the shape. The actin orientation angles in the original model did not contain values for every pixel. Third, we create a larger matrix from the actin orientation angles matrix from the model and added zeros for orientation angles outside the boundary of shape to ensure that this larger matrix matched the same dimension as the matrix from the *in vitro* data. Finally, we obtained a matrix of actin orientation angles that matched the format of the *in vitro* data.

4.2.7 Comparing model vs experiment

The co-orientational order parameter (COOP) [20] was used to compare consistency of subcellular structure orientation in *in vitro* versus *in silico* cardiomyocytes. The COOP ranges from one to zero for perfect consistency to no consistency respectively. Grids of various sizes were placed over the *in silico.* and *in vitro* images of cells and the average actin orientation was calculated in each grid. To be consistent with the previous chapter, 21 µm was chosen to be the large length scale for cells with area ∼1250 μm^2, and 29 µm was the large length scale for cells with area ∼2500 μm^2. For all cells, 1 µm was the small length scale. The overall COOP at the small and large scales was calculated based on a comparison of the *in silico* image to each of the *in vitro* images.

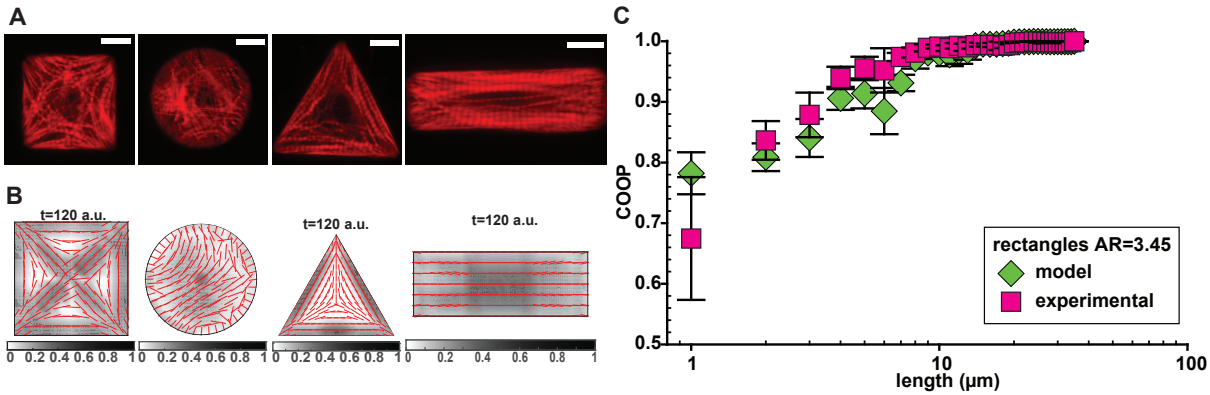

Figure 4.1: **Example of model and experimental cells with area ∼1250 m^2 actin fibril consistency in NRVM**(A) Images of stained NRVMS cultured on various shaped FN islands. The red stain in the images is for actin. (B) Images of actin fibrils in cells created from computational model. (C) The average COOP for consistency of actin fibril organization at different length-scales in rectangular shaped NRVMs with an aspect ratio∼3.5. Scale bars=10 µm.

4.2.8 Statistics

One-way ANOVA with the Holm-Sidak post-hoc test was used to determine statistical significance. Significance was considered for a p-value less than the critical level.

4.3 Results

4.3.1 *In silico* v.s. *in vitro* Cardiomyocytes with Area ∼1250 μm^2

In the previous chapter, we examined how consistency of self-assembly changes within *in vitro* neonatal rat ventricular myocytes (NRVM) of various shapes and aspect ratios (Fig. 4.1A) over multiple length scales. Next, we explored consistency of self-assembly in cardiomyocytes *in silico*. To do this, we used our previously created phenomenological myofibrillogenesis model to create single cardiomyocytes of various shapes (e.g. circles, rectangles, and triangles) and aspect ratios (Fig. 4.1B). Cells with an area of ∼1250 μm^2

from this model (Fig. 4.1B) were compared to *in vitro* data from neonatal rat ventricular myocytes (Fig. 4.1A) over multiple length scales using the co-orientational order parameter (COOP) (Fig. 4.1C). The COOP was calculated in order to quantify consistency of actin fibrils for a variety of length scales in both types of data (Fig. 4.1C).

To be consistent with how we analyzed the results in the previous chapter, we present the results at two length scales, a small length scale (∼1 µm) and a large length scale (∼21 µm) in order to summarize our findings. At the small scale, the consistency of the model matched the consistency of the *in vitro* data (Fig. 4.2A) and there was no significant difference between the model and experimental results. Additionally, at this small scale, the consistency of the model increased as aspect ratio increased (Fig. 4.2A). However, excluding triangular shaped cells with aspect ratios of ∼1.9, the consistency of actin for various shapes of similar aspect ratios from the model was not significantly different. The difference between actin consistency values for triangles with aspect ratios of ∼1.9 was 0.29 which is extremely high compared to the difference in consistency values obtained by other shapes with similar aspect ratios. Thus, there was significant difference between triangular shaped cardiomyocytes from the model with aspect ratios of 1.83 and 1.95. At this small scale, actin consistency for the model settles arounds an aspect ratio of ∼6 with the average consistency for shapes with an $AR > 5.5$ of 0.90. Actin consistency was high for the model at the large length scale (Fig. 4.2B). Excluding circular shaped cells at ∼21 µm, aspect ratio did not affect actin consistency for the model (Fig. 4.2B). The difference between the consistency for circular shaped cells and rectangular shaped cells with an aspect ratio of 1.00 and triangular shaped cells with an aspect ratio of 1.15 was 0.27 and 0.30 respectively. As a result there was significant difference between circular shaped cells and other shapes with similar aspect ratios. None of the model results were significantly different from the *in vitro* data at the large scale. However, at ∼21 µm for the model results, the circular shaped cells were significantly different than the rectangular and triangular shapes with an aspect ratio of ∼1. Actin consistency at ∼21 µm for the rest of the shapes of similar aspect ratios from the

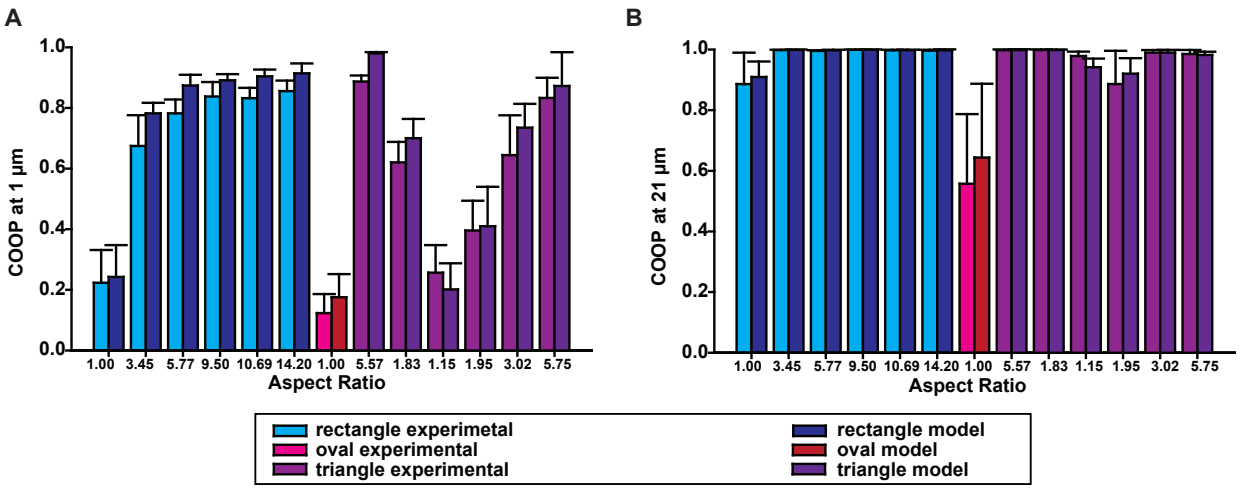

Figure 4.2: **Model and experimental cells with area ∼1250 μm^2 actin fibril consistency for various aspect ratios.**The average COOP for consistency of actin fibril organization in model and experimental cells for different aspect ratios at the small length-scale of ∼1 µm (A) and at the large length-scale ∼21 µm (B).

model was not significantly different.

4.3.2 *In silico* v.s. *in vitro* Cardiomyocytes with Area ∼2500 μm^2

Actin fibril consistency of the model versus experimental results was examined at the small length scale (∼1 µm) (Fig. 4.3A) and at the large length scale (∼21 µm) for cells with an area of ∼2500 μm^2 (Fig. 4.3A). The model exhibited a higher consistency at both of these scales. Also, there was no significant difference between the model and experimental results at either of these scales. Next, we looked at consistency at another large length scale (∼29 µm) determined based on the area of these larger cells (Fig. 4.3A). For most shapes the model displayed higher consistency than the experimental cells. Still, at this scale (∼29 µm) there was no significant difference between the model and experimental results.

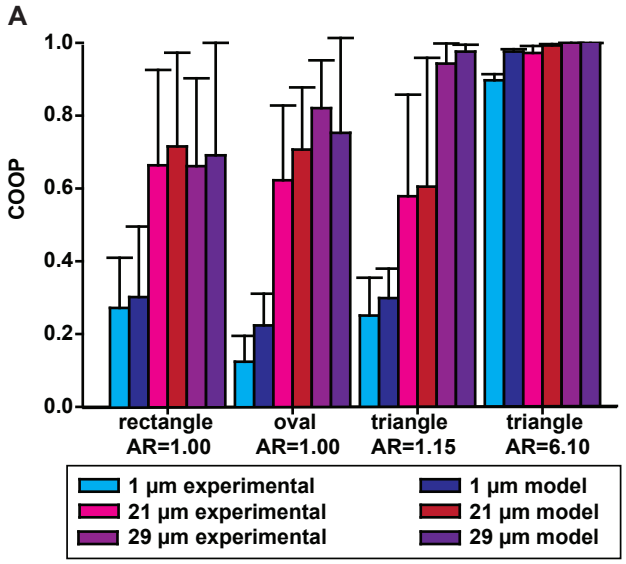

Figure 4.3: **Model and experimental cells with ∼2500 μm^2 actin fibril consistency for various aspect ratios.**(A)The average COOP for consistency of actin fibril organization in model and experimental cells for different aspect ratios at 3 different length-scales: ∼1 µm, ∼21µm, and ∼29 µm.

4.4 Discussion

In this chapter, we created cells from a previous computational myofibrillogenesis model [32] and used to co-orientational order parameter [20] to quantitatively compare actin fibril consistency *in silico* and *in vitro* cardiomyocytes. At the small length scale of ∼1 µm for cardiomyocytes with an area of ∼1250 μm^2 or ∼2500 μm^2 we were able to demonstrate that the model matches experimental results. These result contradicts our hypothesis, we expected the model to be less accurate at the small length scale. This could be due to the fact that the model mostly produce higher consistency values than the *in vitro* data for all the shapes examined at this small scale. Additionally, we showed that the model matched experimental results at the larger scales of ∼21µm, and ∼29 µm as well. Based on our results we can conclude that the model is accurate at both small and large length scales since there was no significant difference between the model results and the experimental result at the three different length scales. Thus, we successfully quantitatively validated our existing model across multiple length scales. Therefore, this provides us with a validation

tool that can be used in the future to build modular additions into our myofibrillogenesis model.

Chapter 5

Summary

This research was set out to explore *in vitro* and *in silico* self-assembly of cardiomyocytes. To investigate this we needed to select a tool to quantify correlation and consistency of subcellular structures. There were a variety of metrics and tools that could have been used to quantify organization of subcellular structures. For instance, previous studies have used different statistical metrics that are based on a variety of distributions [17, 43, 23]. Other studies used different image correlation methods to compare images [15, 25, 54, 35]. Another example of a metric used by previous studies to quantify organization is the orientational order parameter (OOP) [24, 75, 66, 72, 31, 45]. In fact, the OOP has been used to quantify organization in cardiac tissues and cardiomyocytes [31, 45]. However, the OOP is not capable of evaluating the consistency of one subcellular structure or the correlation between two subcellular structures. Therefore, we needed to design a tool that did not depend on certain distributions and was capable of evalutaing consistency of one subcellular structure and the correlation of two subcellular structures. Thus, we created a new tool, the co-orientational order parameter (COOP) to quantify correlation and consistency of subcellular structures. The COOP was developed with similar mathematical framework as the OOP. As an application of the COOP, we compared the orientation of

sarcomeric z-lines and actin fibrils in isotropic engineered cardiac tissues. As a results, we identified the expected perpendicular correlation between actin fibril and sarcomere z-line orientations in isotropic engineered cardiac tissue. In addition, we sought to examined the consistency of subcellular structures at a variety of length scales. Specifically, this study wanted to answer three questions: (1) how does the consistency of subcellular structures (which self-assemble) in cardiomyocytes change in a multi-scale way, (2) how consistency of self-assembly in cardiomyocytes is affected by extracellular matrix (ECM) cues, and (3) how size of the ECM affect consistency of self-assembly?

To answer these questions neonatal rat ventricular myocytes were created in various shapes, sizes, and aspect ratios and the COOP was used to quantify consistency of actin fibrils and sarcomeric z-lines at multiple subcellular length scales. By observing consistency at multuple length scales, we showed that cells with an area of $\sim$1250 μm^2 and high aspect ratios, e.g. elongated cells, without sharp corners produced the highest actin fibril consistency at smaller subcellular length-scales. Therefore, in order for actin fibrils to consistency self-assemble at this small length-scale it is advantageous for cells to be a smooth elongated shape. Additionally, we discovered that the size of the ECM island does not effect self-assembly of actin fibrils. As well as determined that there was distinct spatial scales of self-assembly for actin fibrils. In fact, our results proved that the distinct spatial scales of self-assembly for actin fibrils are constant between similar shapes on different sized ECM islands. Thus, we believe this is evidence proving that the mechanism behind self-assembly is based on a bottom-up assembly.

Finally, we wanted to add length scales into out previously developed myofibrillogenesis model. Previously the model was developed in a modular way and was based on arbitrary units. Once length scales were incorporated into the model, we compared the model to data from *in vitro* cardiomyocytes. In particular, we showed that the our myofibrillogenesis model was accurate for large and small length scales. Therefore, we were able to validate

the incorporation of length scales into our model.

In the future, our parameter could be used to identify the consistency of cytoskeleton organizations at multiple length scales in cells of different origins. As well as determine distinct spatial scales of consistent cytoskeleton organization in a variety of cell sources. In addition, our myofibrillogenesis model could be used as a validation tool in the future to incorporate further modular additions to the model such as the actual presence of sarcomeres or motility. Lastly, we believe the co-orientational order parameter and our myofibrillogenesis model will dramatically impact our ability to build accurate models that predict and explain the behavior of cells of varying sources.

Bibliography

[1] E. Aikawa, P. Whittaker, M. Farber, K. Mendelson, R. F. Padera, M. Aikawa, and F. J. Schoen. Human semilunar cardiac valve remodeling by activated cells from fetus to adult: Implications for postnatal adaptation, pathology, and tissue engineering. *Circulation*, 113(10):1344–1352, 2006.

[2] B. Alberts, A. Johnson, J. Lewis, M. Raff, K. Roberts, and P. Walter. *Molecular Biology of the Cell*. Garland, 4th edition, 2002.

[3] H. Ashikaga, J. C. Criscione, J. H. Omens, J. W. Covell, and J. Ingels, Neil B. Transmural left ventricular mechanics underlying torsional recoil during relaxation. *Am J Physiol Heart Circ Physiol*, 286(2):H640–647, 2004.

[4] H. Ashikaga, J. H. Omens, and J. W. Covell. Time-dependent remodeling of transmural architecture underlying abnormal ventricular geometry in chronic volume overload heart failure. *Am J Physiol Heart Circ Physiol*, 287(5):H1994–2002, 2004.

[5] M. R. Badrossamay, K. Balachandran, A. K. Capulli, H. M. Golecki, A. Agarwal, J. A. Goss, H. Kim, K. Shin, and K. K. Parker. Engineering hybrid polymer-protein super-aligned nanofibers via rotary jet spinning. *Biomaterials*, 35(10):3188–3197, 2014.

[6] K. Balachandran, P. W. Alford, J. Wylie-Sears, J. A. Goss, A. Grosberg, J. Bischoff, E. Aikawa, R. A. Levine, and K. K. Parker. Cyclic strain induces dual-mode endothelial-mesenchymal transformation of the cardiac valve. *Proceedings of the National Academy of Sciences*, 108(50):19943–8, 2011.

[7] E. Batschelet. *Circular Statistics in Biology*. Academic Press, London, 1981.

[8] P. Berens. Circstat: A matlab toolbox for circular statistics. *J Stat Softw*, 31(10):1–21, 2009.

[9] M. A. Bray, S. P. Sheehy, and K. K. Parker. Sarcomere alignment is regulated by myocyte shape. *Cell Motil Cytoskel*, 65(8):641–651, 2008.

[10] M.-A. P. Bray, W. J. Adams, N. A. Geisse, A. W. Feinberg, S. P. Sheehy, and K. K. Parker. Nuclear morphology and deformation in engineered cardiac myocytes and tissues. *Biomaterials*, 31(19):5143–5150, 2010.

[11] N. Bursac, Y. H. Loo, K. Leong, and L. Tung. Novel anisotropic engineered cardiac tissues: Studies of electrical propagation. *Biochemical and Biophysical Research Communications*, 361(4):847–853, 2007.

[12] N. Bursac, K. K. Parker, S. Iravanian, and L. Tung. Cardiomyocyte cultures with controlled macroscopic anisotropy - a model for functional electrophysiological studies of cardiac muscle. *Circulation Research*, 91(12):E45–E54, 2002.

[13] CDC. Heart disease facts, August 10, 2015.

[14] J. J. Chen, W. Liu, H. Y. Zhang, L. Lacy, X. X. Yang, S. K. Song, S. A. Wickline, and X. Yu. Regional ventricular wall thickening reflects changes in cardiac fiber and sheet structure during contraction: quantification with diffusion tensor mri. *American Journal of Physiology-Heart and Circulatory Physiology*, 289(5):H1898–H1907, 2005.

[15] C.-L. Chiu, M. A. Digman, and E. Gratton. Cell matrix remodeling ability shown by image spatial correlation. *Journal of Biophysics*, 2013:8, 2013.

[16] J. N. Cohn, R. Ferrari, and N. Sharpe. Cardiac remodeling—concepts and clinical implications: a consensus paper from an international forum on cardiac remodeling. *Journal of the American College of Cardiology*, 35(3):569–582, 2000.

[17] P. Davidson, M. Bigerelle, B. Bounichane, M. Giazzon, and K. Anselme. Definition of a simple statistical parameter for the quantification of orientation in two dimensions: Application to cells on grooves of nanometric depths. *Acta Biomaterialia*, 6(7):2590–2598, 2010.

[18] V. S. Deshpande, R. M. McMeeking, and A. G. Evans. A bio-chemo-mechanical model for cell contractility. *Proc Natl Acad Sci USA*, 103(45):17065–17065, 2006.

[19] V. S. Deshpande, M. Mrksich, R. M. McMeeking, and A. G. Evans. A bio-mechanical model for coupling cell contractility with focal adhesion formation. *J Mech Phys Solids*, 56(4):1484–1510, 2008.

[20] N. K. Drew, M. A. Eagleson, D. B. Baldo Jr, K. K. Parker, and A. Grosberg. Metrics for assessing cytoskeletal orientational correlations and consistency. *PLoS Comput Biol*, 11(4):e1004190, 2015.

[21] N. K. Drew and A. Grosberg. *Methods of Myofibrillogenesis Modeling*, pages 75–91. Springer New York, New York, NY, 2015.

[22] A. P. Du, J. M. Sanger, and J. W. Sanger. Cardiac myofibrillogenesis inside intact embryonic hearts. *Developmental Biology*, 318(2):236–246, 2008.

[23] G. A. Dunn and A. F. Brown. Alignment of fibroblasts on grooved surfaces described by a simple geometric transformation. *Journal of Cell Science*, 83:313–340, 1986.

[24] A. W. Feinberg, P. W. Alford, H. Jin, C. M. Ripplinger, A. A. Werdich, S. P. Sheehy, A. Grosberg, and K. K. Parker. Controlling the contractile strength of engineered cardiac muscle by hierarchal tissue architecture. *Biomaterials*, 2012.

[25] Z. Feng, H. Qingming, and G. Wen. Image matching by normalized cross-correlation. In *2006 IEEE International Conference on Acoustics Speech and Signal Processing Proceedings*, volume 2, pages II–II.

[26] N. T. Feric and M. Radisic. Maturing human pluripotent stem cell-derived cardiomyocytes in human engineered cardiac tissues. *Advanced Drug Delivery Reviews*, 96:110–134, 2016.

[27] A. S. Forouhar, M. Liebling, A. Hickerson, A. Nasiraei-Moghaddam, H.-J. Tsai, J. R. Hove, S. E. Fraser, M. E. Dickinson, and M. Gharib. The embryonic vertebrate heart tube is a dynamic suction pump. *Science*, 312(5774):751–753, 2006.

[28] N. A. Geisse, S. P. Sheehy, and K. K. Parker. Control of myocyte remodeling in vitro with engineered substrates. *In Vitro Cell Dev-An*, 45(7):343–350, 2009.

[29] A. M. Gerdes and J. M. Capasso. Structural remodeling and mechanical dysfunction of cardiac myocytes in heart failure. *Journal of Molecular and Cellular Cardiology*, 27(3):849–856, 1995.

[30] S. Göktepe, O. J. Abilez, K. K. Parker, and E. Kuhl. A multiscale model for eccentric and concentric cardiac growth through sarcomerogenesis. *Journal of Theoretical Biology*, 265(3):433–442, 2010.

[31] A. Grosberg, P. W. Alford, M. L. McCain, and K. K. Parker. Ensembles of engineered cardiac tissues for physiological and pharmacological study: Heart on a chip. *Lab on a Chip*, 11(24):4165–4173, 2011.

[32] A. Grosberg, P. L. Kuo, C. L. Guo, N. A. Geisse, M. A. Bray, W. J. Adams, S. P. Sheehy, and K. K. Parker. Self-organization of muscle cell structure and function. *PLoS Computational Biology*, 7(2), 2011.

[33] X. Guo, A. E. K. Hutcheon, S. A. Melotti, J. D. Zieske, V. Trinkaus-Randall, and J. W. Ruberti. Morphologic characterization of organized extracellular matrix deposition by ascorbic acid–stimulated human corneal fibroblasts. *Investigative Ophthalmology & Visual Science*, 48(9):4050–4060, 2007.

[34] I. W. Hamley. *Introduction to soft matter : synthetic and biological self-assembling materials*. John Wiley and Sons, Chichester, England ;Hoboken, NJ, rev. edition, 2007.

[35] B. Hanson, K. Klink, K. Matsuura, S. M. Robeson, and C. J. Willmott. Vector correlation: Review, exposition, and geographic application. *Annals of the Association of American Geographers*, 82(1):103–116, 1992.

[36] P. Helm, M. F. Beg, M. I. Miller, and R. L. Winslow. Measuring and mapping cardiac fiber and laminar architecture using diffusion tensor mr imaging. *Ann NY Acad Sci*, 1047(1):296–307, 2005.

[37] P. A. Helm, L. Younes, M. F. Beg, D. B. Ennis, C. Leclercq, O. P. Faris, E. McVeigh, D. Kass, M. I. Miller, and R. L. Winslow. Evidence of structural remodeling in the dyssynchronous failing heart. *Circ Res*, 98(1):125–132, 2006.

[38] L. Hong, Y. F. Wan, and A. Jain. Fingerprint image enhancement: Algorithm and performance evaluation. *Ieee Transactions on Pattern Analysis and Machine Intelligence*, 20(8):777–789, 1998.

[39] J. Ivaska. Unanchoring integrins in focal adhesions. *Nat Cell Biol*, 14(10):981–983, 2012.

[40] C. L. Ives, S. G. Eskin, and L. V. McIntire. Mechanical effects on endothelial cell morphology: in vitro assessment. *In vitro cellular & developmental biology : journal of the Tissue Culture Association*, 22(9):500–7, 1986. 3759792.

[41] R. K. Iyer, L. L. Y. Chiu, L. A. Reis, and M. Radisic. Engineered cardiac tissues. *Current Opinion in Biotechnology*, 22(5):706–714, 2011.

[42] M. K. B. Jonsson, M. A. Vos, G. R. Mirams, G. Duker, P. Sartipy, T. P. de Boer, and T. A. B. van Veen. Application of human stem cell-derived cardiomyocytes in safety pharmacology requires caution beyond herg. *Journal of Molecular and Cellular Cardiology*, 52(5):998–1008, 2012.

[43] W. J. Karlon, P. P. Hsu, S. Li, S. Chien, A. D. McCulloch, and J. H. Omens. Measurement of orientation and distribution of cellular alignment and cytoskeletal organization. *Annals of Biomedical Engineering*, 27(6):712–720, 1999.

[44] K. Kartasalo, R.-P. Pölönen, M. Ojala, J. Rasku, J. Lekkala, K. Aalto-Setälä, and P. Kallio. Cytospectre: a tool for spectral analysis of oriented structures on cellular and subcellular levels. *BMC Bioinformatics*, 16(1):1–23, 2015.

[45] M. B. Knight, N. K. Drew, L. A. McCarthy, and A. Grosberg. Emergent global contractile force in cardiac tissues. *Biophysical Journal*, 110(7):1615–1624, 2016.

[46] P. Kovesi. Matlab and octave functions for computer vision and image processing, 2005.

[47] P.-L. Kuo, H. Lee, M.-A. Bray, N. A. Geisse, Y.-T. Huang, W. J. Adams, S. P. Sheehy, and K. K. Parker. Myocyte shape regulates lateral registry of sarcomeres and contractility. *The American Journal of Pathology*, 181(6):2030–2037, 2012.

[48] W. J. Larsen. *Development of the Heart*, pages 131–155. W. B. Saunders Company, 2nd edition, 1997.

[49] M. Liebling, A. S. Forouhar, R. Wolleschensky, B. Zimmermann, R. Ankerhold, S. E. Fraser, M. Gharib, and M. E. Dickinson. Rapid three-dimensional imaging and analysis of the beating embryonic heart reveals functional changes during development. *Developmental Dynamics*, 235(11):2940–2948, 2006. 10.1002/dvdy.20926.

[50] M. L. McCain, S. P. Sheehy, A. Grosberg, J. A. Goss, and K. K. Parker. Recapitulating maladaptive, multiscale remodeling of failing myocardium on a chip. *Proceedings of the National Academy of Sciences*, 110(24):9770–9775, 2013.

[51] J. M. Molitoris, S. Paliwal, R. B. Sekar, R. Blake, J. Park, N. A. Trayanova, L. Tung, and A. Levchenko. Precisely parameterized experimental and computational models of tissue organization. *Integrative Biology*, 8(2):230–242, 2016.

[52] E. E. Morrill, A. N. Tulepbergenov, C. J. Stender, R. Lamichhane, R. J. Brown, and T. J. Lujan. A validated software application to measure fiber organization in soft tissue. *Biomechanics and Modeling in Mechanobiology*, pages 1–12, 2016.

[53] D. Mozaffarian, E. J. Benjamin, A. S. Go, D. K. Arnett, M. J. Blaha, M. Cushman, S. R. Das, S. de Ferranti, J.-P. Després, H. J. Fullerton, V. J. Howard, M. D. Huffman, C. R. Isasi, M. C. Jiménez, S. E. Judd, B. M. Kissela, J. H. Lichtman, L. D. Lisabeth, S. Liu, R. H. Mackey, D. J. Magid, D. K. McGuire, E. R. Mohler, C. S. Moy, P. Muntner, M. E. Mussolino, K. Nasir, R. W. Neumar, G. Nichol, L. Palaniappan, D. K. Pandey, M. J. Reeves, C. J. Rodriguez, W. Rosamond, P. D. Sorlie, J. Stein, A. Towfighi, T. N. Turan, S. S. Virani, D. Woo, R. W. Yeh, and M. B. Turner. Heart disease and stroke statistics—2016 update. *A Report From the American Heart Association*, 2015.

[54] A. Noorafshan, S. Karbalay-Doust, H. Khazraei, A. Rafati, and H. Mirkhani. Spatial arrangement of the heart structure: Application of second-order stereology in diabetic rats. *Annals of Anatomy - Anatomischer Anzeiger*, 196(1):20–25, 2014.

[55] I. L. Novak, B. M. Slepchenko, A. Mogilner, and L. M. Loew. Cooperativity between cell contractility and adhesion. *Phys Rev Lett*, 93(26 Pt 1):268109, 2004.

[56] P. W. Oakes, S. Banerjee, M. C. Marchetti, and M. L. Gardel. Geometry regulates traction stresses in adherent cells. *Biophysical Journal*, 107(4):825–833, 2014.

[57] M. J. Paszek, D. Boettiger, V. M. Weaver, and D. A. Hammer. Integrin clustering is driven by mechanical resistance from the glycocalyx and the substrate. *PLoS Comput Biol*, 5(12), 2009.

[58] T. Pong, W. J. Adams, M.-A. Bray, A. W. Feinberg, S. P. Sheehy, A. A. Werdich, and K. K. Parker. Hierarchical architecture influences calcium dynamics in engineered cardiac muscle. *Experimental Biology and Medicine*, 236(3):366–373, 2011.

[59] A. Romero-Munoz, L. Maffei, E. Cuellar, and A. J. Noss. Temporal separation between jaguar and puma in the dry forests of southern bolivia. *Journal Tropical Ecology*, 26:303–311, 2010.

[60] J. W. Sanger, S. M. Kang, C. C. Siebrands, N. Freeman, A. P. Du, J. S. Wang, A. L. Stout, and J. M. Sanger. How to build a myofibril. *J Muscle Res Cell M*, 26(6-8):343–354, 2005.

[61] S. P. Sheehy, A. Grosberg, and K. K. Parker. The contribution of cellular mechanotransduction to cardiomyocyte form and function. *Biomechanics and Modeling in Mechanobiology*, 11(8):1227–1239, 2012.

[62] S. P. Sheehy, F. Pasqualini, A. Grosberg, S. J. Park, Y. Aratyn-Schaus, and K. K. Parker. Quality metrics for stem cell-derived cardiac myocytes. *Stem Cell Reports*, 2(3):282–294, 2014.

[63] M. S. Spach, J. F. Heidlage, R. C. Barr, and P. C. Dolber. Cell size and communication: Role in structural and electrical development and remodeling of the heart. *Heart Rhythm*, 1(4):500–515, 2004.

[64] M. S. Spach, J. F. Heidlage, P. C. Dolber, and R. C. Barr. Electrophysiological effects of remodeling cardiac gap junctions and cell size: Experimental and model studies of normal cardiac growth. *Circulation Research*, 86(3):302–311, 2000.

[65] D. D. Streeter Jr., H. M. Spotnitz, D. P. Patel, J. Ross, and E. H. Sonnenblick. Fiber orientation in the canine left ventricle during diastole and systole. *Circulation Research*, 24:339–347, 1969.

[66] J. G. Sun, J. Tang, and J. D. Ding. Cell orientation on a stripe-micropatterned surface. *Chinese Science Bulletin*, 54(18):3154–3159, 2009.

[67] K. Takahashi and S. Yamanaka. Induction of pluripotent stem cells from mouse embryonic and adult fibroblast cultures by defined factors. *Cell*, 126(4):663–676, 2006.

[68] J. L. Tan, W. Liu, C. M. Nelson, S. Raghavan, and C. S. Chen. Simple approach to micropattern cells on common culture substrates by tuning substrate wettability. *Tissue Eng*, 10(5-6):865–872, 2004.

[69] A. Tondon and R. Kaunas. The direction of stretch-induced cell and stress fiber orientation depends on collagen matrix stress. *PLoS ONE*, 9(2):e89592, 2014.

[70] F. Torrent-Guasp, M. J. Kocica, A. F. Corno, M. Komeda, F. Carreras-Costa, A. Flotats, J. Cosin-Aguillar, and H. Wen. Towards new understanding of the heart structure and function. *European Journal of Cardio-Thoracic Surgery*, 27(2):191–201, 2005.

[71] J. Torzewski, M. Torzewski, D. E. Bowyer, M. Fröhlich, W. Koenig, J. Waltenberger, C. Fitzsimmons, and V. Hombach. C-reactive protein frequently colocalizes with the terminal complement complex in the intima of early atherosclerotic lesions of human coronary arteries. *Arteriosclerosis, Thrombosis, and Vascular Biology*, 18(9):1386–1392, 1998.

[72] A. Umeno and S. Ueno. Quantitative analysis of adherent cell orientation influenced by strong magnetic fields. *IEEE Trans Nanobiosci*, 2(1):26–28, 2003.

[73] M. Vendelin, P. Bovendeerd, J. Engelbrecht, and T. Arts. Optimizing ventricular fibers: Uniform strain or stress, but not atp consumption, leads to high efficiency. *American Journal of Physiology*, 283:1072–1081, 2002.

[74] M. Vey, S. Pilkuhn, H. Wille, R. Nixon, S. DeArmond, E. Smart, R. Anderson, A. Taraboulos, and S. Prusiner. Subcellular colocalization of the cellular and scrapie prion proteins in caveolae-likemembranousdomains. *Proceedings of the National Academy of Sciences*, 93(25):14945–14949, 1996.

[75] D. Volfson, S. Cookson, J. Hasty, and L. S. Tsimring. Biomechanical ordering of dense cell populations. *Proceedings of the National Academy of Sciences of the United States of America*, 105(40):15346–15351, 2008.

[76] X. Wang, H. Osinska, G. W. Dorn, M. Nieman, J. N. Lorenz, A. M. Gerdes, S. Witt, T. Kimball, J. Gulick, and J. Robbins. Mouse model of desmin-related cardiomyopathy. *Circulation*, 103(19):2402–2407, 2001.

[77] A. Wax, C. H. Yang, V. Backman, K. Badizadegan, C. W. Boone, R. R. Dasari, and M. S. Feld. Cellular organization and substructure measured using angle-resolved low-coherence interferometry. *Biophysical Journal*, 82(4):2256–2264, 2002.

[78] M. B. Youngquist and M. D. Boone. Movement of amphibians through agricultural landscapes: The role of habitat on edge permeability. *Biol Conserv*, 175:148–155, 2014.

[79] A. Zaritsky, U. Obolski, Z. Kadlecova, Z. Gan, Y. Du, S. L. Schmid, and G. Danuser. Decoupling global and local relations in biased biological systems. *bioRxiv*, 2016.

Appendix A

COOP

A.1 Orientational Order Parameter (OOP)

The OOP characterizes the order of orientation of a single construct. For disordered systems the OOP is zero and for perfectly aligned systems it is one. The OOP is calculated by using a set of vectors, $\overrightarrow{p_i}$, and forming a tensor for each of the vectors. The mean tensor is:

$$\mathbb{T} = \left\langle 2 \begin{bmatrix} p_{i,x}p_{i,x} & p_{i,x}p_{i,y} \\ p_{i,x}p_{i,y} & p_{i,y}p_{i,y} \end{bmatrix} - \begin{bmatrix} 1 & 0 \\ 0 & 1 \end{bmatrix} \right\rangle = \{Mean\ tensor\}. \tag{A.1}$$

The OOP is defined as the maximum eigenvalue of the mean tensor

$$\begin{aligned} OOP &= \max\left[\text{eigenvalue}(\mathbb{T})\right] = \{Orientational\ order\ parameter\} \\ &= \left\langle 2\{\overrightarrow{p_i} \cdot \hat{n_p}\right\}^2 - 1\right\rangle = \left\langle \cos\left(2(\alpha - \alpha_0)\right)\right\rangle \end{aligned} \tag{A.2}$$

where $\hat{\text{n}}_\text{p}$ and α_0 are the director and mean angle, respectively.

A.2 Symmetry of OOP

The OOP also has pseudo-vector symmetry and this can be easily shown.To check for symmetry we need to vary the sign of $\overrightarrow{p_i}$ and $\hat{\mathrm{n}}_{\mathrm{p}}$. If we change the sign of $\overrightarrow{p_i}$, $\hat{\mathrm{n}}_{\mathrm{p}}$ or both we obtain:

$$\Big\langle 2\Big\{-\overrightarrow{p_i}\cdot\hat{n_p}\Big\}^2-1\Big\rangle=\Big\langle 2\Big\{\overrightarrow{p_i}\cdot\big(-\hat{n_p}\big)\Big\}^2-1\Big\rangle=\Big\langle 2\Big\{-\overrightarrow{p_i}\cdot\big(-\hat{n_p}\big)\Big\}^2-1\Big\rangle=\Big\langle 2\{\overrightarrow{p_i}\cdot\hat{n_p}\Big\}^2-1\Big\rangle. \tag{A.3}$$

Thus, we will produce the same OOP no matter the sign of $\overrightarrow{p_i}$ and $\hat{\mathrm{n}}_{\mathrm{p}}$ therefore the OOP is symmetric.

A.3 Second order correlations

The OOP is not able to characterize second order correlations. To prove this define P as:

$$\overrightarrow{p_i}=\Big[\cos(\frac{\pi}{2})),\sin(\frac{\pi}{2}))\Big] \text{ and } \overrightarrow{p}_{i+n}=\Big[\cos(-\frac{\pi}{2}),\sin(-\frac{\pi}{2})\Big] \tag{A.4}$$

for i = 1, ..., n. Thus, ($\hat{n}_p=0$ and $\alpha_0=0$):

$$OOP_P=\sum_{i=1}^{2n}\cos(2\alpha)=n\cdot\cos\Big(2\frac{\pi}{2}\Big)+n\cdot\cos\Big(2\big(-\frac{\pi}{2}\big)\Big)=0. \tag{A.5}$$

Thus, OOP=0 even though there is obvious organization in P.

A.4 Circular Statistics (assume period of π)

It is possible to show that the R of circular statistics [8] is the same as the OOP. If the data is distributed:

$$\alpha = \frac{2\pi x}{k} \tag{A.6}$$

where, x is the data in the original scale, k is the total number of steps on the x scale, and α is the variable on the new directional scale (i.e. with a standard 2π period). In our case a rod that is β degrees away from the director is physically the same rod as the one $\beta + \pi$ degrees away. Therefore in our case $k = \pi$ and:

$$\alpha = 2\theta \tag{A.7}$$

where, θ is defined as the angle that we measured from the director. From this it follows:

$$S = \frac{1}{N}\sum_{i=1}^{N} \sin 2\theta_i \tag{A.8}$$

$$C = \frac{1}{N}\sum_{i=1}^{N} \cos 2\theta_i \tag{A.9}$$

$$R = \sqrt{S^2 + C^2}. \tag{A.10}$$

If we assume that the director is orientated such that $\theta_{\hat{n}} = 0$, then the angles are evenly distributed between positive and negative and therefore $S = 0$. We can then write R as:

$$R = C = \frac{1}{N}\sum_{i=1}^{N} \cos 2\theta_i = \langle \cos 2\theta_i \rangle. \tag{A.11}$$

Therefore, by definition of the director we will have the range $0 < R < 1$ and it is equivalent

to the $OOP = 2\langle\cos^2\theta_i\rangle - 1 = \langle\cos 2\theta_i\rangle = R$.

A.5 Circular Correlation

In the special case, with both constructs having a uniform distribution, i.e. both being perfectly isotropic, the correlation coefficient and COOP converge to the same equation. If the angles are uniformally distributed on the circle the correlation coefficient [7] can be written as

$$r = \sqrt{\left(\frac{1}{N}\sum_{i=1}^{N}\cos 2\theta_i\right)^2 + \left(\frac{1}{N}\sum_{i=1}^{N}\sin 2\theta_i\right)^2} \tag{A.12}$$

where θ represents the angle between two biological constructs. If the director is to be assumed $\hat{n}$=[1,0] then $\langle\sin 2\theta_i\rangle = 0$, and therefore

$$r = \sqrt{\left(\frac{1}{N}\sum_{i=1}^{N}\cos 2\theta_i\right)^2} = \langle\cos 2\theta_i\rangle. \tag{A.13}$$

Thus, $COOP = 2\langle\cos^2\theta_i\rangle - 1 = \langle\cos 2\theta_i\rangle = r$.

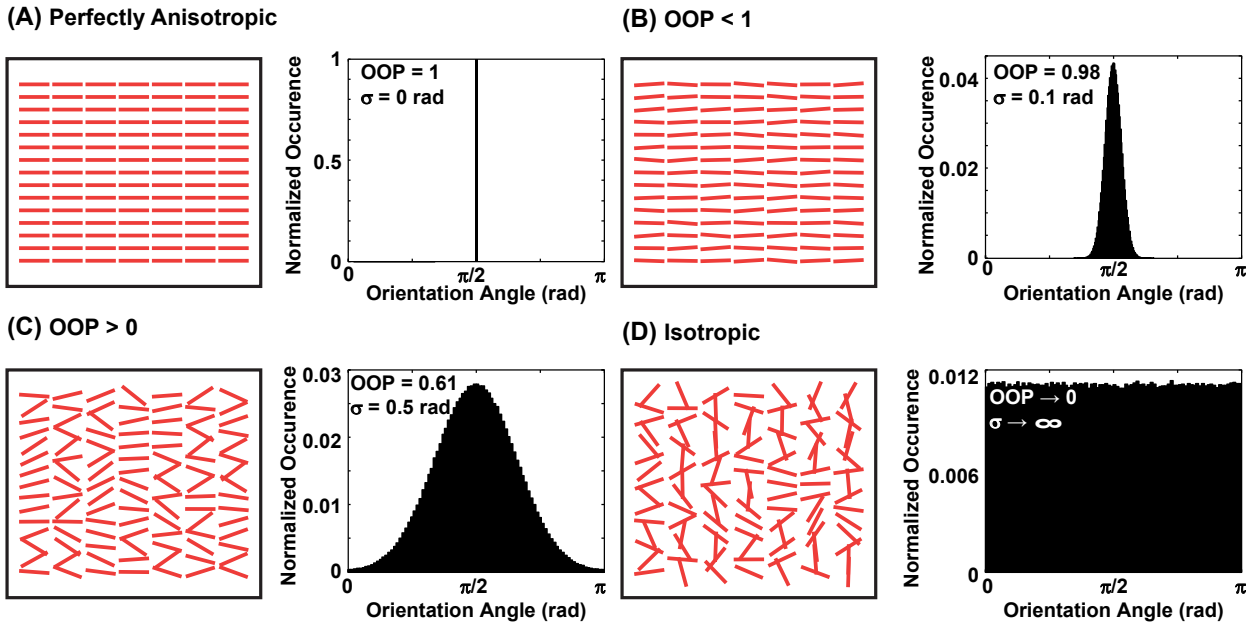

Figure A.1: **Example of OOP using synthetic data.** For (A-D) schematic of the construct is on the left, and the orientation distribution with the OOP and standard deviation is on the right. (A) Perfect alignment; (B) almost perfect organization; (C) somewhat anisotropic; (D) perfectly isotropic.

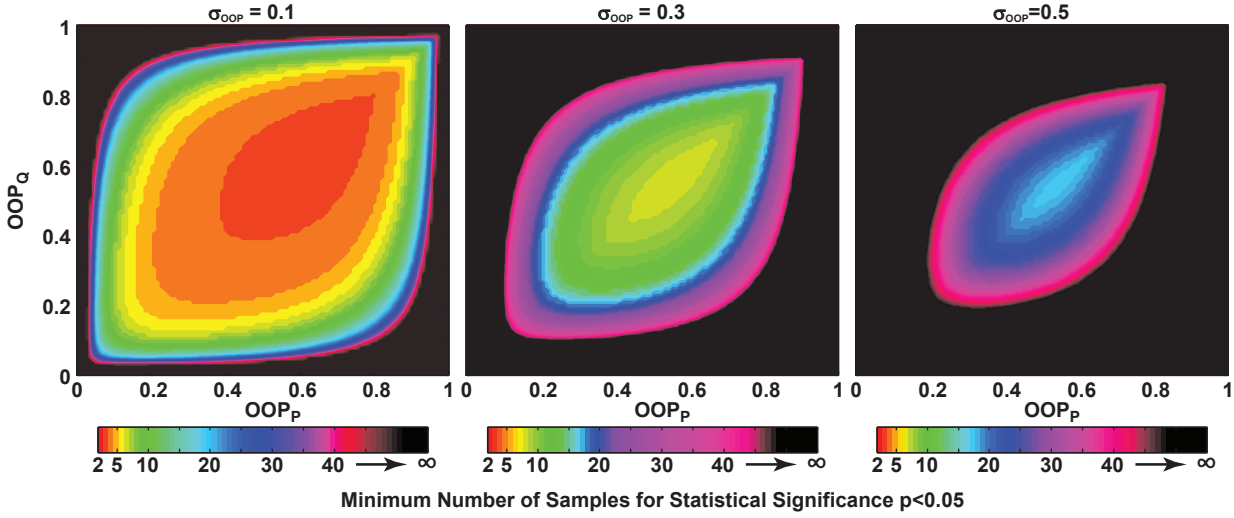

Figure A.2: **Minimum Sample Size.** Statistical significance at p<0.05, with OOP error of σ_{OOP} =0.1, σ_{OOP} =0.3, and σ_{OOP} =0.5.

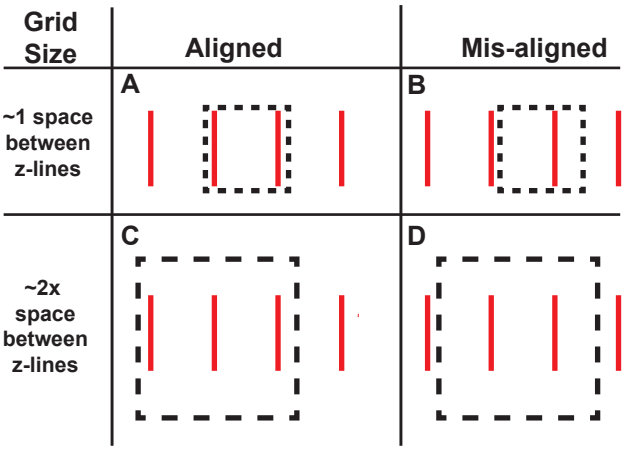

Figure A.3: **Schematic for grid size selection.** For (A-D) schematic of square grids (dashed black line outlines) on Z-lines(red). (A-B) Grid size equivalent to one sarcomere complex length. (C-D) Grid size equivalent to two sarcomere complex length. (A,C) Grid by chance aligns with Z-lines. (B,D) Grid does not align with Z-lines. we choose the grids shown in C-D because we cannot control the alignment of grid to sarcomere complex.

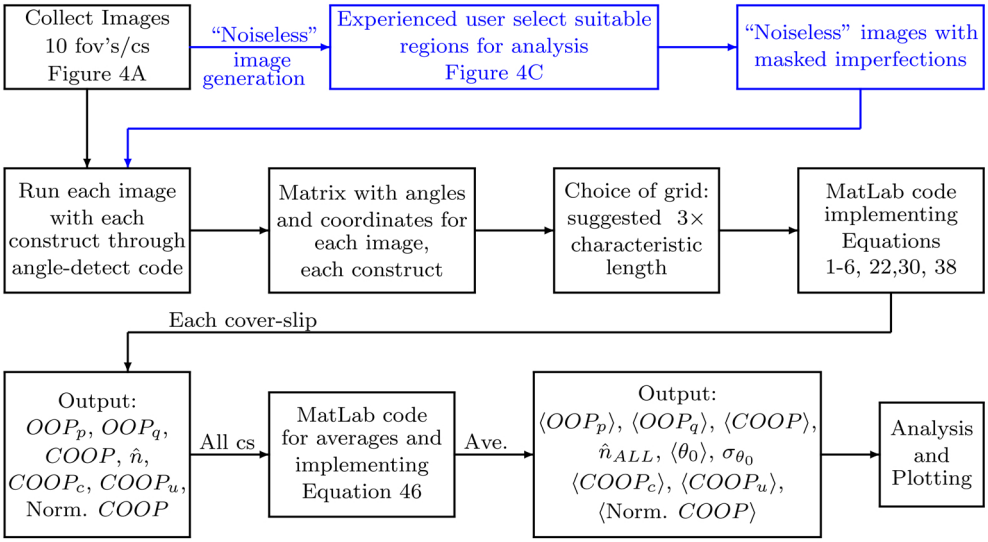

Figure A.4: **Implementation Flow Chart.** Flow chart sketching the implementation of the new method for experimental data. The additional steps for generating "noiseless" images with minimal imperfection is highlighted in blue.

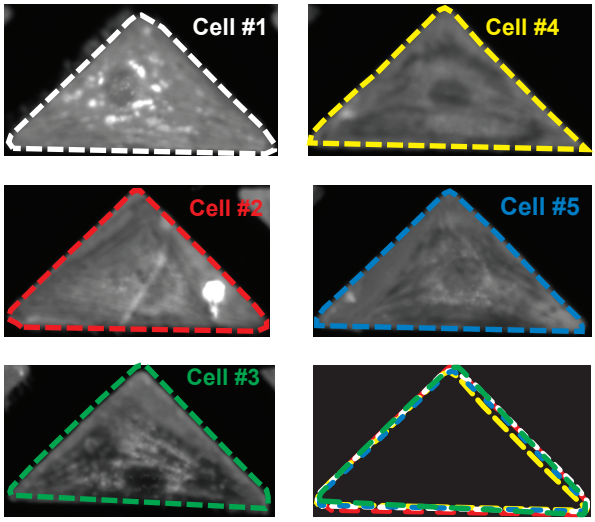

Figure A.5: **Fibronectin stains.** Image of the fibronectin island for each cell in Fig. 2.4I were cropped such that the triangular islands aligned with each other.